THESIS FOR THE DEGREE OF DOCTOR OF PHILOSOPHY
IN
THERMO AND FLUID DYNAMICS

Turbomachinery Aeroacoustic Calculations using Nonlinear Methods

MARTIN OLAUSSON

Division of Fluid Dynamics

Department of Applied Mechanics

CHALMERS UNIVERSITY OF TECHNOLOGY

Göteborg, Sweden, 2011

Turbomachinery Aeroacoustic Calculations using Nonlinear Methods
MARTIN OLAUSSON
ISBN 978-91-7385-481-8

Doktorsavhandling vid Chalmers tekniska högskola
Ny serie nr 3162
ISSN 0346-718X

Division of Fluid Dynamics
Department of Applied Mechanics
Chalmers University of Technology
SE-412 96 Göteborg, Sweden

Phone: +46-(0)31-7721400
Fax: +46-(0)31-180976

Printed at Chalmers Reproservice
Göteborg, Sweden, 2011

Turbomachinery Aeroacoustic Calculations using Non-linear Methods

MARTIN OLAUSSON

Division of Fluid Dynamics
Department of Applied Mechanics
Chalmers University of Technology

Abstract

Noise regulations for aircraft that fly over populated areas are becoming continuously stricter. This in combination with increasing computational capabilities has boosted interest in aeroacoustic computations in the aerospace industry. New numerical methods that are able to predict noise will play a major role in future aircraft and engine designs, and validation and possibly improvements of these new methods are needed for results with satisfying accuracy.

This thesis shows how nonlinear blade row interaction computations that focus on aeroacoustics can be made in an accurate and efficient way. It is shown how the computations of a succession of blade rows with non-matching blade count can be made more efficient by utilizing the chorochronic periodicity.

The tonal acoustic response from a stator vane with rotor wake impingement is calculated with the chorochronic method and compared to a linear method, and the results are in good agreement. The harmonic balance technique was also tested for tone noise predictions and shows a good potential to be a more efficient tool than using standard time stepping for obtaining periodic solutions. The Newton-GMRES method is shown to be a suitable algorithm for obtaining convergence and for better performance of the harmonic balance computations.

Broadband noise predictions from rotor wake impingement on stators are calculated with a hybrid RANS/LES method and chorochronic buffer zones. The noise is evaluated with a FWH surface integral method.

Keywords: Computational Aeroacoustics, CAA, Computational Fluid Dynamics, CFD, Hybrid RANS/LES, Acoustic analogies, Ffowcs-Williams & Hawkings, FWH, Rotor-Stator interaction, Fan-Noise, Tone, Broadband, Chorochronic periodicity, Time lag, Nonlinear, Harmonic Balance Technique, Time Spectral, Newton-GMRES, Buffer layer, Sponge, Counter-Rotating Propfan, Oscillating sphere

List of Publications

This thesis is based on the work contained in the following papers:

I M. Olausson, L.-E. Eriksson and S. Baralon, 2007, Evaluation of Nonlinear Rotor Wake/Stator Interaction by using Time Domain Chorochronic Solver, *The 8th ISAIF meeting*, July 2-5, Lyon, France

II M. Olausson, L.-E. Eriksson and S. Baralon, 2007, Nonlinear Rotor Wake/Stator Interaction Computations, *The 18th ISABE meeting*, September 2-7, Beijing, China

III M. Olausson, L.-E. Eriksson, 2009, Rotor Wake/Stator Broadband Noise Calculations Using Hybrid RANS/LES and Chorochronic Buffer Zones, *15th AIAA/CEAS Aeroacoustics Conference*, 11-13 May, Miami, Florida, (AIAA 2009-3338)

IV M. Olausson, L.-E. Eriksson, 2009, An Absorbing Inlet Buffer Layer for Rotor Wake/Stator Time Domain Computations, *Proceedings of ASME Turbo Expo 2009*, June 8-12, Orlando, Florida, USA, (GT2009-59346)

V M. Olausson, L.-E. Eriksson, 2010, Absorbing Inlet Boundary Analysis of Rotor Wake/Stator Time Domain Computations, *16th AIAA /CEAS Aeroacoustics Conference*, 7-9 June, Stockholm, Sweden, (AIAA-2010-3882)

VI M. Olausson, R. Avellán, N. Sörman, F. Rudebeck, L.-E. Eriksson, 2010, Aeroacoustics and Performance Modeling of a Counter-Rotating Propfan, *Proceedings of ASME Turbo Expo 2010*, June 14-18, Glasgow, UK, (GT2010-22543)

Division of work between authors

The work leading to this thesis was done in collaboration with other researchers. The respondent is the first author of all the papers on which this thesis is based. The work on the nonlinear results in Papers I and II was done by the respondent and the linear calculations were made by Dr Stéphane Baralon. The 3D mode analysis tool used in Papers IV and V was provided by Dr Mattias Billson. The numerical analysis was made by the respondent in Paper VI, but the design of the blades, the performance calculations and the numerical mesh were made by Niklas Sörman and Filip Rudebeck under the supervision of the respondent and Richard Avellán. The theoretical work and code development presented in the papers were carried out in discussions with the supervisor, Professor Lars-Erik Eriksson.

Acknowledgments

This work was supported by NFFP (National Aeronautical Research Program) in Sweden and the FLOCON project (Adaptive and Passive Flow Control for Fan Broadband Noise Reduction) supported by the European Union under the Seventh Framework, Grant agreement no.: 213411. It was carried out at the Department of Applied Mechanics, Division of Fluid Dynamics, at Chalmers University of Technology in collaboration with Volvo Aero Corporation.

The computations in this thesis have been done primarily at three different computer centers: Chalmers Center for Computational Science and Engineering (C3SE), the High Performance Computing Center North (HPC2N) and the National Supercomputer Centre (NSC) in Linköping. The Swedish National Infrastructure for Computing (SNIC) is acknowledged for granting access to HPC2N and NSC.

I would like to thank my supervisor Lars-Erik Eriksson for all his guidance and help through these years working toward a Ph.D. Many thanks to my co-supervisor Stéphane Baralon for good reflections and contributions to my work during the early years. I would also like to thank my colleagues at the Division of Fluid Dynamics who helped to create a fun and inspiring working environment, especially Markus, Fredrik, Richard, Lei, Walter and Tobias for making the conference trips unforgettable. Thanks also to my colleagues at Volvo Aero Corporation, especially Mattias Billson for his valuable help with the code development in the last years and Jonas Larsson for help during the work reported in Paper VI. Andreas Lundström is also acknowledged for all our interesting Wednesday afternoon discussions over a sandwich. Finally and most importantly, I would like to thank Ellen for loving me and being my best friend.

Nomenclature

Latin symbols

a	amplitude
b	constant in low-pass filter
c	speed of sound
C_p	specific heat at constant pressure
$C_{\varepsilon 1}$	constant in the k-epsilon turbulence model
$C_{\varepsilon 2}$	constant in the k-epsilon turbulence model
C_μ	constant in the k-epsilon turbulence model
D_{t_l}	coefficients in time spectral derivative
e	internal energy
$\mathcal{F}_j$	Cartesian components of flux vector
f	frequency
G	time stepping routine
$\mathcal{H}$	source vector
$\bar{H}_m$	Hessenberg matrix
J	Jacobian matrix
J_m	Bessel functions of first kind
k	stator BPF index, turbulent kinetic energy
k_x	wave number
l_t	turbulent length scale
m	circumferential mode number, number of Krylov vectors
M	Mach number
M_r	Mach number relative to observer
$\mathbf{M}$	Mach number vector
N_b	number of blades
N_h	number of harmonics
N_{tl}	number of time levels
n	rotor BPF index
n_i	Cartesian component of wall normal vector
$\mathbf{n}$	wall normal vector
p	pressure
P_k	turbulent production term
Pr	laminar Prandtl number

Pr_t	turbulent Prandtl number
Q	state vector in flow equations on conservative form
$\mathcal{Q}$	characteristic number
q	state vector in flow equations on primitive form
R	annular shell radius
r	radial coordinate, residual, distance from source to observer
s	shape parameter
S^*	spectral time derivative source term
S_{ij}	strain rate tensor
t	time
T	temperature, period
$\mathcal{T}$	transformation matrix
u_i	Cartesian components of velocity vector
v_i	Krylov vectors, Cartesian component of velocity vector
v_n	wall normal component of velocity vector
$\mathbf{v}$	velocity vector
W	characteristic variables
x	state vector containing all DOF
x_0	start vector containing all DOF
x_i	Cartesian coordinate vector component
$\mathbf{x}$	observer position
$\mathbf{x}_s$	integration point on surface / in volume
Y_m	Bessel functions of second kind

Greek symbols

α	angle between observer and wall normal vector
δ_{ij}	Kronecker delta
ϵ	damping factor
ε	dissipation of turbulent kinetic energy, small number
κ	characteristic number
λ	wavelength, residual smoothing constant
μ	laminar dynamic viscosity, radial mode number
μ_t	turbulent eddy viscosity
Ω	angular velocity, rotor shaft speed
ω	angular frequency $(\omega = 2\pi f)$
Φ	Fourier coefficients of state vector
ϕ	Fourier coefficients of the primitive variables in cylindrical coordinate system
Π	complex amplitude of pressure
ρ	density
σ	hub-to-tip ratio
σ_k	constant in the k-epsilon turbulence model
σ_ε	constant in the k-epsilon turbulence model

τ	pseudo time, residence time
τ_{ij}	viscous stress tensor
θ	circumferential coordinate

Subscripts

0	total condition
θ	circumferential component
l	time level index
r	radial component
t	turbulent quantity
x	axial component
∞	surrounding state

Superscripts

$'$	fluctuating component
$-$	ensemble averaged quantity
$\sim$	Favre-filtered ensemble averaged quantity
$\hat{}$	Fourier representation
N	number of time steps
p	time step index

Abbreviations

BPF	blade passing frequency
BPR	bypass ratio
CAA	computational aeroacoustics
CC	combustion chamber
CFD	computational fluid dynamics
CFL	Courant-Friedrich-Lewy
DNS	direct numerical simulation
DOF	degrees of freedom
FPR	fan pressure ratio
FWH	Ffowcs-Williams & Hawkings
GMRES	generalized minimal residual method
LES	large eddy simulation
LNSE	linearized Navier-Stokes equations
MPI	message passing interface
OGV	outlet guide vane
RANS	Reynolds-averaged Navier-Stokes

Contents

Paper I

Paper II

Paper III

Paper IV

Paper V

Paper VI

Chapter 1

Introduction

1.1 Motivation

TURBOMACHINERY NOISE is a common disturbing phenomenon to which people are exposed almost everywhere in modern society. Turbomachinery is defined as a machine that transfers energy from a rotor to a fluid and vice versa. In everyday life, this would be your vacuum cleaner, hairdryer, the fan in your computer etc. It is in the nature of something that rotates and pushes on a fluid to generate noise. The exception may be a slowly rotating rotor that operates in a uniform flow field, where the flow on the rotor blades surfaces is laminar, and where there are no objects downstream of the rotor that are affected by the nonuniform flow field caused by the rotor itself. No noise is generated in that case, but this is unfortunately not the case in most practical applications. Most turbomachines operate in environments where the rotors are surrounded by objects that disturb the flow and where turbulence exists in the flow upstream of the rotor and is created by the rotor. The surfaces of the machine that face the fluid will therefore experience unsteady flow fields in terms of turbulence, large scale velocity fluctuations or pressure fluctuations, which in turn generate noise. This work focuses on flow induced noise that is generated by aircraft engines, although the methods described here can also be applied to other turbomachines.

As more and more transports are carried out by aircraft, and as the areas around airports become more and more populated, the noise pollution caused by air traffic becomes an increasing problem. As a result of this, regulations[1] have been proposed by the International Civil Aviation Organization (ICAO) for how much community noise can be acceptable around airports. In combination with local restrictions

[1]Volume I of Annex 16 to the Convention on International Civil Aviation

at airports with heavy traffic, this has made noise an important issue for aircraft and engine manufacturers. Noise must now be considered early in the design process of new aircrafts and engines to ensure that acceptable levels are met without costly redesigns at late stages. A key element in accomplishing this is accurate and efficient prediction tools.

In addition to reducing noise, future aircraft must also be more fuel efficient in order to minimize the overall negative environmental impact. One important factor in the commonly used turbofan engine, depicted in figure 1.1, is the propulsion efficiency, which can be increased by reducing the fan pressure ratio (FPR). More air has to pass through the fan to achieve the same amount of thrust when the FPR is reduced, and this is done by increasing the diameter of the fan, hence increasing the bypass ratio (BPR). Increasing fan diameter has been a main trend since the introduction of jet engines in commercial aviation. As the diameter increases, so does the drag from the nacelle. An up-to-date question is whether the turbofan can be replaced by one without a nacelle, i.e. an unducted fan/propfan. The diameter can then be increased even more and the FPR further reduced without increasing nacelle drag. There is no longer a protective shroud around the blades though, and because of this there will be higher structural demands on the blades for safety reasons. The main concern, however, is noise since the shroud can no longer be used to suppress it.

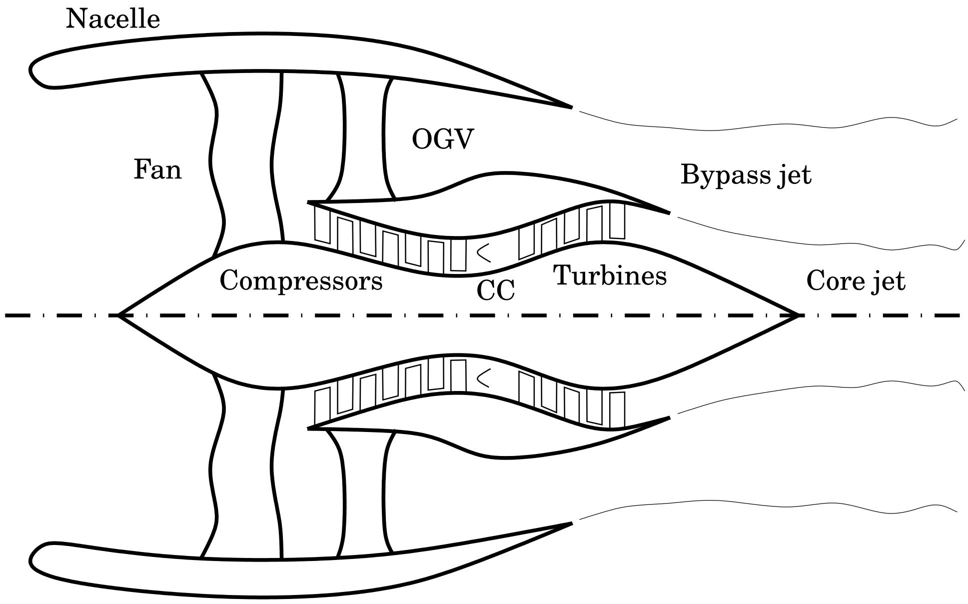

Figure 1.1: Basic components of a turbofan engine.

In commercial air transportation the crucial operating points in terms of noise are take-off and approach, since the distance between the source and populated areas is relatively short. At cruise conditions, the distance to the ground is far enough for the noise to attenuate as long as the aircraft is operating at a subsonic speed. What may be of concern during cruise is the cabin noise, even though not regulated, since passenger comfort is an important marketing issue, although this has mainly been a problem for propeller-powered airplanes. The flow-induced noise sources that are present when an aircraft is in operation can be divided into two main categories: airframe noise and engine noise. The first category includes noise generated by the aircraft fuselage and the trailing edge noise of the wings. The first category also includes the noise produced by the flow around landing gears and high lift devices. These noise sources may contribute as much as the engines to the community noise during near ground operation. The second category includes jet noise, core noise and turbomachinery noise. The jet noise is caused by the turbulent mixing process in the jet behind the engine and is highly dependent on the velocity of the jet. The jet velocity is reduced when the FPR is reduced and the move towards more efficient engines thus also leads to a reduction in jet noise. The core noise is generated by the combustion process inside the engine and may under certain circumstances, e.g. engine idle, be the dominant noise source.

The main source of turbomachinery noise in an aircraft engine is the fan. It typically operates with a supersonic tip Mach number during take-off and a subsonic tip Mach number during approach. The noise characteristics will be very different in these two operating conditions due to a rotor-locked shock wave system that forms around the blades at supersonic relative blade velocities. The shock waves couple to the duct in a nonlinear fashion. This will be very sensitive to small blade to blade differences and radiate from the inlet as multiple pure tones or “buzz saw” noise (Hubbard, 1994). The rotor alone will also create noise of a broadband character, mainly from the trailing edges of the blades, at both subsonic and supersonic tip speeds. Outlet guide vanes (OGVs) are placed in the bypass duct to recover the energy of the swirl in the flow downstream of the rotor. The unsteady aerodynamic interaction between the fan and the OGVs is another important source of turbomachinery noise and is the main focus of this thesis. The rotor wakes that are generated from the boundary layer on the rotor blades, i.e. the rotor’s trace in the flow downstream of the rotor, will impinge on the stators as shown in figure 1.2 and create unsteady pressure fluctuations on the vanes that produce noise of both a broadband and a tonal character. The broadband part of the noise is generated by the turbulence in the wake and the tonal part is produced by the periodicity of the rotor wakes and the stators. It is the blade passing frequency (BPF) that is the fundamental frequency of a rotor-stator interaction, if turbulence and other unsteady secondary flow features are neglected, and the tonal noise will consist of the BPF and its harmonics. This is the key to simplifying calculations of tone noise; the following chapters will explain how it is done. The thesis also includes *a priori* broadband noise predictions where the aim is to resolve the "medium" scale turbulence in the rotor wake and to model the small scales.

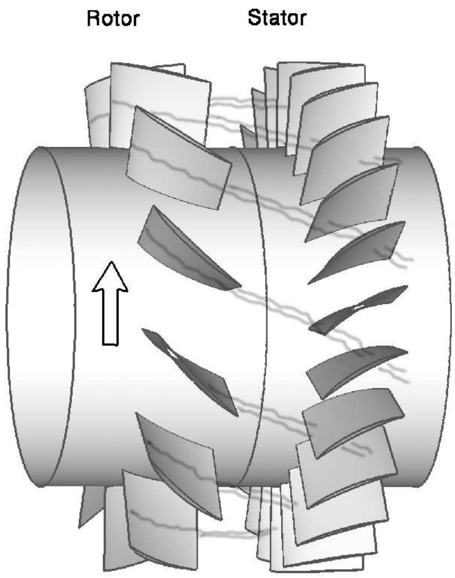

Figure 1.2: Rotor-stator configuration. The flow goes from left to right and the arrow indicates that the rotor spins counter-clockwise. The shadowed lines show the approximate instantaneous rotor wake position at mid radius, and the wakes spin at the same speed and direction as the rotor.

The goal of the work in this thesis is to make efficient and accurate aeroacoustic predictions of rotor-stator interactions. This goal is broken down into three main objectives:

1.1.1 Thesis Objectives

Explore and utilize a few promising methods for efficient and accurate numerical predictions of nonlinear aerodynamic blade row interactions. Focus on aeroacoustics and general methods for blade rows with non-matching blade count. This includes finding appropriate methods for both tone and broadband noise predictions.

Apply suitable methods for reducing reflections at the inflow and outflow boundaries of the computational domain. The flow path will be cut and computations will be made on truncated domains. Acoustic and vorticity waves must be able to leave the domain and be absorbed by the boundary condition. Unsteady waves may also be artificially damped before they reach the inflow or outflow boundaries as a means for avoiding spurious reflections at the boundary.

Investigate the use of acoustic analogies for improving the quality and efficiency of the noise predictions. The computational cost can be reduced by making the unsteady aerodynamic computation on a truncated domain and then integrate the noise sources to the farfield by using an acoustic analogy.

1.2 Rotor-Stator Interactions

The interaction between a set of two blade rows follows the theory developed by Tyler & Sofrin (1962):

$$m = nN_{b,rotor} + kN_{b,stator} \tag{1.1}$$

where

$$\begin{aligned} n &= 1, 2, 3... \\ k &= ... - 1, 0, 1... \end{aligned} \tag{1.2}$$

This equation gives information about what kind of deterministic flow disturbances can be created from the interaction between a set of two blade rows, with N_{rotor} number of rotor blades and N_{stator} number of stator vanes. The disturbances are divided into circumferential modes (or spinning modes), m; an example of a circumferential mode with $m = 8$ is shown in figure 1.3. The spinning modes created from the rotor alone are $m = nN_{rotor}$ and the flow is periodic and stationary in the rotor frame of reference if turbulent fluctuations are averaged. When these modes, e.g. rotor wakes, interact with the stator vanes, all combinations of modes according to eq. (1.1) are created. The sign of m determine the direction in which each mode spins. The frequency of these modes in the stator frame of reference is determined by:

$$\omega_n = nN_{b,rotor}\Big(\Omega_{rotor} - \Omega_{stator}\Big) \tag{1.3}$$

where $n = 1$ gives the rotor BPF and higher values yield multiples of it. The frequency controls the speed at which the modes spin because one circumferential wave length must pass a fixed point during one period. Modes with higher values of m must therefore spin more slowly for the same frequency. This is important when acoustic modes are considered, because all combinations of m will not propagate in a duct. This will be discussed in the next section.

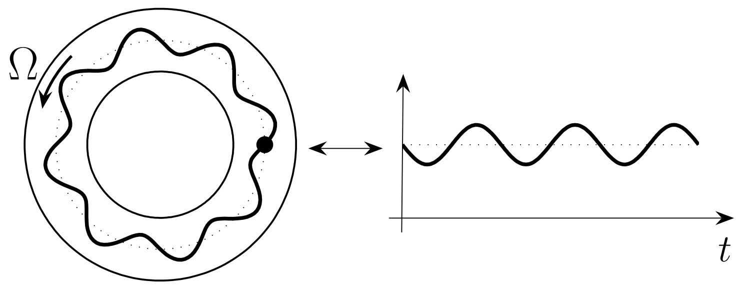

Figure 1.3: Spinning lobed pattern with circumferential mode number $m = 8$ inside an annular duct. The angular velocity, Ω, of the pattern and the value of m determine the frequency of the mode and vice versa.

1.3 Acoustic Duct Modes

1.3.1 Thin Annular Duct

Pressure modes from a rotor-stator interaction in a thin annular duct can be represented as spinning modes of the form

$$p(x, \theta, t) = \sum_n \sum_k \Pi_{n,k} e^{i\omega_n t} e^{-im\theta} e^{-ik_{x_m} x} \tag{1.4}$$

in the stator frame of reference if radial variations are neglected. Coefficients $\Pi_{n,k}$ are complex numbers specifying the amplitude and phase for each mode. The circumferential mode number, m, is calculated from eq. (1.1) and the frequency is calculated as in eq. (1.3). The axial wave number can be calculated as

$$k_{x_m} = \frac{m}{R}\sqrt{(M_m^\theta)^2 - 1} \tag{1.5}$$

if there is no mean flow in the duct. Variable R is the annular duct radius and M_m^θ is the Mach number of the mode pattern in the circumferential direction, calculated as

$$M_m^\theta = \frac{R\omega_n}{mc} \tag{1.6}$$

where c is the speed of sound. An acoustic mode must spin with a circumferential Mach number that is equal to or larger than unity in order to propagate and eventually radiate to the surroundings. The mode will otherwise decay exponentially in the axial direction since the axial wave number becomes complex. Propagating and non-propagating modes are called cut-on and cut-off modes, respectively. Another way of looking at it is that, for a given frequency, the acoustic mode must have enough space in the circumferential direction for at least the mode number times the wave length, $m\lambda$, in order to propagate.

For a given stage, it is the combinations of n and k yielding the lowest values of m that gives the cut-on modes. Thus in designs for low tone noise, the number of stator vanes is usually much higher than the number of rotor blades. In this way, cut-on modes of fundamental frequency, which contain the most energy, are avoided. On the other hand, the broadband noise usually increases with an increased number of stators. One solution is to have fewer vanes, to accept some "low" frequency cut-on acoustic modes and then to have tuned liners (noise suppressors) in the duct to damp them before they radiate to the surroundings.

1.3.2 General Annular Duct

Another way to reduce noise is to modify the radial variations of the acoustic spinning modes inside a duct of finite height. All circumferential modes can be decomposed into radial modes and different modes can be excited by modifying the shape of the vane, e.g. lean or sweep. Each radial mode has its own propagation criteria and a quieter design can be obtained by shifting as much energy as possible to radial modes that are cut-off. The theory behind radial modes was well described by Tyler & Sofrin (1962). A short summary follows here.

The pressure modes generated by a rotor-stator interaction in a duct with axial flow, i.e. no swirl, can be represented as

$$p\left(x,r,\theta,t\right) = \sum_n \sum_k \sum_\mu \Pi_{n,k,\mu} e^{i\omega_n t} e^{-im\theta} e^{-ik_{x\mu}x} E_{m\mu}^\sigma\left(\kappa_{m\mu}^\sigma r\right) \tag{1.7}$$

when radial variations are included and where

$$E_{m\mu}^\sigma\left(\kappa_{m\mu}^\sigma r\right) = J_m\left(\kappa_{m\mu}^\sigma r\right) + \mathcal{Q}_{m\mu}^\sigma Y_m\left(\kappa_{m\mu}^\sigma r\right) \tag{1.8}$$

is the characteristic function to the solution of the wave equation inside the duct. It consists of the sum of the Bessel function of the first kind, J_m, and the weighted Bessel function of the second kind, Y_m. The shape of the characteristic function will depend on both the circumferential and radial mode index as well as with the hub-to-tip ratio:

$$\sigma = \frac{R_{hub}}{R_{shroud}} \tag{1.9}$$

If the fluid is at rest, i.e. there is no mean flow, the axial wave number for a radial mode can be formulated as

$$k_{x_\mu} = \frac{m}{R_{shroud}} \sqrt{\left(M_m^\theta \left(R_{shroud}\right)\right)^2 - \left(\frac{\kappa_{m\mu}^{*\sigma}}{m}\right)^2} \tag{1.10}$$

where $M_m^\theta \left(r_{shroud}\right)$ is the circumferential Mach number of the mode at the shroud wall. To find out whether or not a mode is propagating, i.e. a real or imaginary wave number, it is necessary to find the characteristic numbers

$$\kappa_{m\mu}^{*\sigma} = \left\{ \kappa_{m\mu}^{\sigma} r = R_{shroud} \kappa_{m\mu}^{\sigma} \frac{r}{R_{shroud}} = \kappa_{m\mu}^{*\sigma} r^* \right\} = R_{shroud} \kappa_{m\mu}^{\sigma} \tag{1.11}$$

and $\mathcal{Q}_{m\mu}^{\sigma}$ from the eigenvalue problem

$$\begin{array}{l} J_m^{'}\left(\ \kappa_{m\mu}^{*\sigma}\right) + \mathcal{Q}_{m\mu}^{\sigma} Y_m^{'}\left(\ \kappa_{m\mu}^{*\sigma}\right) = 0 \\ J_m^{'}\left(\sigma\kappa_{m\mu}^{*\sigma}\right) + \mathcal{Q}_{m\mu}^{\sigma} Y_m^{'}\left(\sigma\kappa_{m\mu}^{*\sigma}\right) = 0 \end{array} \tag{1.12}$$

where the primes denote differentiation with respect to argument. While the equation for the axial wave number in the three dimensional case, eq. (1.10), is a bit more difficult to interpret than the two dimensional equation (1.5), the result is similar. The criteria necessary for a radial mode, $m\mu$, to propagate is that the tip circumferential Mach number of the pattern must still be supersonic, although the exact limit depends on m, μ and σ. The radial modes in a nonuniform mean flow or a swirling flow must be found numerically, and it is then impractical to use Bessel functions to describe the radial variations (Verdon, 2001).

1.4 Computational Aeroacoustics

Aeroacoustic noise can be calculated from first principles by direct numerical simulations (DNS) of the compressible Navier-Stokes equations. This was done for jet noise by e.g. Freund (2001) for a relatively low Reynolds number. The equations are then discretized in time and space and all turbulence structures must be resolved by the computational mesh. The sound waves also need to be resolved, but the wave lengths of these are usually larger than the size of the eddies. For high Reynolds number flow, as in a full scale aircraft engine, the computational cost of making DNS is too high with today's computers, and models for the small scale turbulence are needed to allow for the use of a coarser mesh. Two different approaches are used in this thesis, where the first aims to model all turbulent fluctuations and the second aims only to model the turbulent fluctuations that are not resolved by the mesh. The first approach will be used to calculate the deterministic/tone noise from the aerodynamic interaction of a rotor-stator configuration, i.e. the Tyler & Sofrin interaction modes, while the second approach is used to capture some of the turbulent/broadband noise.

Chapter 2

Methodology

2.1 Computational Fluid Dynamics

THIS thesis presents some methods for simulation of rotor-stator interactions. The main tool is a compressible computational fluid dynamics (compressible CFD) code developed by Eriksson (1995). The code solves the Navier-Stokes equations, which describe the flow of a fluid including pressure waves, both in a stationary and a rotating frame of reference. The code is suitable for aeroacoustic calculations, CAA, since it is compressible, as long as all sound sources and pressure waves of interest are captured by the computational mesh.

2.1.1 Unsteady RANS

The Unsteady Favre-filtered Reynolds-averaged Navier-Stokes (URANS) equations in conservative form with a realizable k-epsilon turbulence model can be written in compact form as

$$\frac{\partial Q}{\partial t} + \frac{\partial \mathcal{F}_j}{\partial x_j} = \mathcal{H} \tag{2.1}$$

where the state vector in conservative form is

$$Q = \begin{bmatrix} \overline{\rho} \\ \overline{\rho}\tilde{u}_i \\ \overline{\rho}\tilde{e}_0 \\ \overline{\rho}\tilde{k} \\ \overline{\rho}\tilde{\varepsilon} \end{bmatrix} \tag{2.2}$$

Here $\overline{\rho}$ is the ensemble averaged density, and $\tilde{u}_i$, $\tilde{e}_0$, $\tilde{k}$ and $\tilde{\varepsilon}$ are the Favre-filtered velocity vector, total internal energy, turbulence kinetic energy and turbulence dissipation respectively. The flux vector can be written as

$$\mathcal{F}_j = \begin{bmatrix} \overline{\rho}\tilde{u}_j \\ \overline{\rho}\tilde{u}_i\tilde{u}_j + \overline{p}\delta_{ij} - \tau_{ij} \\ \overline{\rho}\tilde{e}_0\tilde{u}_j + \overline{p}\tilde{u}_j - C_p\left(\left(\frac{\mu}{Pr} + \frac{\mu_t}{Pr_t}\right)\frac{\partial \tilde{T}}{\partial x_j}\right) - \tilde{u}_i\tau_{ij} \\ \overline{\rho}\tilde{k}\tilde{u}_j - \left(\mu + \frac{\mu_t}{\sigma_k}\right)\frac{\partial \tilde{k}}{\partial x_j} \\ \overline{\rho}\tilde{\varepsilon}\tilde{u}_j - \left(\mu + \frac{\mu_t}{\sigma_\varepsilon}\right)\frac{\partial \tilde{\varepsilon}}{\partial x_j} \end{bmatrix} \tag{2.3}$$

where $\overline{p}$ is the ensemble averaged pressure, τ_{ij} is the viscous stress tensor, C_p is the specific heat at constant pressure, μ and μ_t are laminar and turbulence viscosity, Pr and Pr_t are laminar and turbulence Prandtl number, $\tilde{T}$ is the Favre-filtered temperature, and σ_k and σ_ε are constants in the k-epsilon turbulence model. The viscous stress tensor is approximated with a Boussinesq assumption as

$$\tau_{ij} = (\mu + \mu_t)\left(2\tilde{S}_{ij} - \frac{2}{3}\frac{\partial \tilde{u}_k}{\partial x_k}\delta_{ij}\right) - \frac{2}{3}\overline{\rho}\tilde{k}\delta_{ij} \tag{2.4}$$

where $\tilde{S}_{ij}$ is the Favre-filtered strain rate tensor defined as

$$\tilde{S}_{ij} = \frac{1}{2}\left(\frac{\partial \tilde{u}_i}{\partial x_j} + \frac{\partial \tilde{u}_j}{\partial x_i}\right) \tag{2.5}$$

The source vector is defined as

$$\mathcal{H} = \begin{bmatrix} 0 \\ 0 \\ 0 \\ P_k - \overline{\rho}\tilde{\varepsilon} \\ \left(C_{\varepsilon 1}P_k - C_{\varepsilon 2}\overline{\rho}\tilde{\varepsilon}\right)\frac{\tilde{\varepsilon}}{\tilde{k}} \end{bmatrix} \tag{2.6}$$

where P_k is the turbulence production term, and $C_{\varepsilon 1}$ and $C_{\varepsilon 2}$ are constants in the k-epsilon turbulence model. The turbulence production term is approximated as

$$P_k = \left(\mu_t\left(2\tilde{S}_{ij} - \frac{2}{3}\frac{\partial \tilde{u}_k}{\partial x_k}\delta_{ij}\right) - \frac{2}{3}\overline{\rho}\tilde{k}\delta_{ij}\right)\frac{\partial \tilde{u}_i}{\partial x_j} \tag{2.7}$$

Finally, the turbulence viscosity is calculated with a realizability constraint as

$$\mu_t = \min\left(C_\mu\overline{\rho}\frac{\tilde{k}^2}{\tilde{\varepsilon}}, \frac{0.4\overline{\rho}\tilde{k}}{\sqrt{\tilde{S}_{ij}\tilde{S}_{ij}}}\right) \tag{2.8}$$

Table 2.1: Constants in the k-epsilon turbulence model

C_μ	$C_{\varepsilon 1}$	$C_{\varepsilon 2}$	σ_k	σ_ε	Pr_t
0.09	1.44	1.92	1.0	1.3	0.9

where C_μ is a constant in the k-epsilon turbulence model. The various constants in the turbulence model are listed in table 2.1. These equations are solved, assuming a calorically perfect gas, using a finite volume solver based on the G3D family of codes developed by Eriksson (1995). The discretization of the domain is done with a boundary-fitted, curvilinear, non-orthogonal multi-block mesh, and the fluxes are reconstructed with either a standard third-order upwind scheme or a low dissipation third-order upwind scheme for the convective part and a second-order centered difference scheme for the diffusive part. Upwinding is done to make sure that the scheme is stable and it is made on the characteristic variables to ensure that the extra numerical dissipation is as small as possible. The solution is updated with a three-stage Runge-Kutta technique. The solver is parallelized using MPI libraries to enable multi-processor computations. Details on the solver and the MPI implementation are given in Eriksson (1995); Andersson (2005); Stridh (2006). It is assumed in Papers I,II,IV,V and VI that there is a scale separation between the predicted unsteady effects and turbulent fluctuations, and a limit on the length scale is therefore introduced. This limit is further reduced in Paper III to allow for turbulent fluctuations that are resolved by the mesh to evolve without too much influence from the turbulence model. This is often called a hybrid RANS/LES method and is described in the next section.

2.1.2 Hybrid RANS/LES

Hybrid methods can be used if detailed information about the large scale turbulent fluctuations is of interest, and these eddies should then be resolved by the mesh. It is important to use a scheme with low dissipation to make sure that as small eddies as possible are resolved by the mesh. A low dissipation third-order upwind scheme is used in Paper III. This is a fourth-order scheme with minimal amount of upwinding to make the scheme stable (Eriksson, 1995; Andersson, 2005).

The turbulence length scale in the k-epsilon model is at the same time limited to about 20% of a typical cell size. It can be shown that the turbulence model then works as a Smagorinsky subgrid scale LES model everywhere except close to solid walls, where the increased resolution results in a local URANS model. Yan *et al.* (2005) did similar work for a k-omega model. The k-epsilon model is derived as follows:

The turbulence viscosity is defined as

$$\mu_t = C_\mu \overline{\rho} \frac{\tilde{k}^2}{\tilde{\varepsilon}} \tag{2.9}$$

without the realizability constraint. The turbulence length scale is defined as

$$l_t = C_\mu^{3/4} \frac{\tilde{k}^{3/2}}{\tilde{\varepsilon}} \tag{2.10}$$

Taking only the turbulence part of the viscous stress tensor from eq. (2.4) gives:

$$\tau_{ij}^{(t)} = \mu_t \left(2\tilde{S}_{ij} - \frac{2}{3}\frac{\partial \tilde{u}_k}{\partial x_k}\delta_{ij} \right) - \frac{2}{3}\overline{\rho}\tilde{k}\delta_{ij} \tag{2.11}$$

Since the stress tensor is symmetric, the turbulence production term can be written as

$$P_k = \tau_{ij}^{(t)} \frac{\partial \tilde{u}_i}{\partial x_j} = \left\{ \begin{array}{c} \tau_{ij}^{(t)} = \\ Symmetric \end{array} \right\} = \tau_{ij}^{(t)} \tilde{S}_{ij} \tag{2.12}$$

If compressibility effects are moderate, we may approximate the stress tensor as

$$\tau_{ij}^{(t)} = 2\mu_t \tilde{S}_{ij} \tag{2.13}$$

which gives:

$$P_k = 2\mu_t \tilde{S}_{ij}\tilde{S}_{ij} \tag{2.14}$$

It is safe to assume equilibrium conditions for subgrid scale turbulence, which means that the turbulence production is

$$P_k = \overline{\rho}\,\tilde{\varepsilon} \tag{2.15}$$

The dissipation can then be written as

$$\tilde{\varepsilon} = \frac{2\,\mu_t}{\overline{\rho}} \tilde{S}_{ij}\tilde{S}_{ij} \tag{2.16}$$

The turbulence dissipation wants to stay at the lowest possible value when there is an active upper limit on the length scale. This is difficult to prove, but numerical experiments show that this is the case and, together with eq. (2.10), this gives:

$$\tilde{\varepsilon} = C_\mu^{3/4} \frac{\tilde{k}^{3/2}}{l_{t,max}} \tag{2.17}$$

Combining eq. (2.16) with eq. (2.17) gives:

$$C_\mu^{3/4} \frac{\tilde{k}^{3/2}}{l_{t,max}} = \frac{2\,\mu_t}{\overline{\rho}} \tilde{S}_{ij}\tilde{S}_{ij} \tag{2.18}$$

Using eq. (2.17) μ_t can be expressed as follows:

$$\mu_t = C_\mu\,\overline{\rho}\,\frac{\tilde{k}^2}{\tilde{\varepsilon}} = l_{t,max}\,C_\mu^{1/4}\,\overline{\rho}\,\sqrt{\tilde{k}} \tag{2.19}$$

Equations (2.18) and (2.19) give:

$$C_\mu^{3/4} \frac{\tilde{k}^{3/2}}{l_{t,max}} = \frac{2\,l_{t,max}\,C_\mu^{1/4}\,\overline{\rho}\,\sqrt{\tilde{k}}}{\overline{\rho}} \tilde{S}_{ij}\tilde{S}_{ij} \tag{2.20}$$

Rearranging this equation gives an expression for the turbulence kinetic energy:

$$\tilde{k} = \frac{2}{\sqrt{C_\mu}}\,l_{t,max}^2\,\tilde{S}_{ij}\tilde{S}_{ij} \tag{2.21}$$

Combining eq. (2.19) with eq. (2.21) gives an expression for the turbulence viscosity:

$$\mu_t = \sqrt{2}\,\overline{\rho}\,l_{t,max}^2\sqrt{\tilde{S}_{ij}\tilde{S}_{ij}} \tag{2.22}$$

Replacing μ_t in eq. (2.16) with the expression in eq. (2.22) gives:

$$\tilde{\varepsilon} = 2\,\sqrt{2}\,l_{t,max}^2\left(\tilde{S}_{ij}\tilde{S}_{ij}\right)^{3/2} \tag{2.23}$$

This should be compared with a Smagorinsky model (incompressible version):

$$\mu_t = \rho\,(C_S\Delta f)^2\,\sqrt{2\,\tilde{S}_{ij}\tilde{S}_{ij}} \tag{2.24}$$

where C_S is between 0.065 and 0.25 depending on flow and Δf is the filter length scale. By comparing the expressions for μ_t, eq. (2.22) and (2.24), the following relation can be obtained:

$$l_{t,max} = C_S\Delta f \tag{2.25}$$

The filter length scale, Δf, is usually set to some cell size $\Delta f \approx \Delta x$. Typically, $l_{t,max} \approx 0.1\Delta x - 0.2\Delta x$, but $0.2\Delta x$ is preferred here. Note again that $l_{t,max}$ is in the hybrid RANS/LES calculations set to a global value so that the increased resolution close to walls results in a local URANS model.

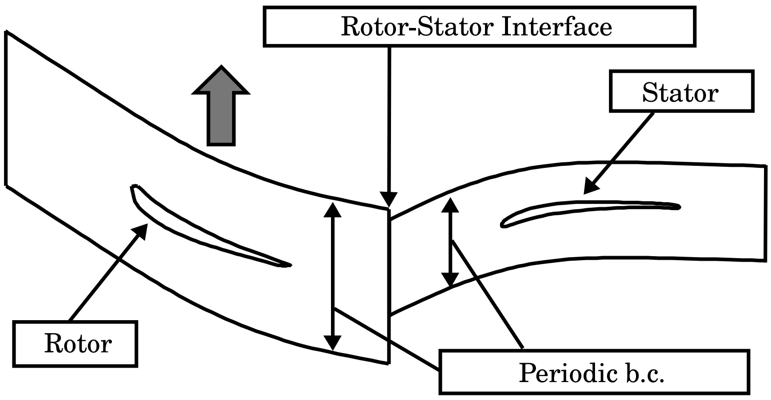

Figure 2.1: A schematic drawing of the computational domains in a rotor-stator computation. The rotor domain is solved in a rotating frame of reference and a rotor-stator interface is used between the rotating and the stationary domain. Periodic boundary conditions are used at the pitchwise boundaries.

2.2 Rotor-Stator Computations

The periodicity in a blade row is often utilized to make the computational domain smaller, i.e. to decrease computational load. This means that the domain for which the flow is solved will contain only one or a few of the rotor blades and one or a few of the stator vanes. Periodic boundary conditions are used in the blade to blade and vane to vane directions. The flow around the rotor is usually solved in a rotating frame of reference, and some kind of interface is needed between the rotor domain and the stator domain to transfer the information from the rotating to the stationary frame of reference. A schematic of a rotor-stator computation with one blade per blade row is shown in figure 2.1.

The most commonly used rotor-stator interface is the mixing-plane interface that averages the flow properties in the circumferential direction. It should be noted that by using this type of approach, all unsteady interactions are lost. This is still used in aerodynamic design calculations since the time it takes to make a steady computation compared to an unsteady is often at least one order of magnitude less and the unsteady interactions are not as important for aerodynamic design. In aeroacoustics, however, capturing the unsteady interactions is of great importance. Another method is the frozen-rotor approach, where the rotor flow is transformed to the stator frame of reference and the rotor wake is kept, but not rotating. Again, the unsteady interaction is lost since this is also a steady computation.

If the number of blades and vanes is the same, then the domains have the same size in the circumferential direction, and a sliding grid interface can be used to capture the unsteady rotor-stator interaction. The flow variables are interpolated and converted from the rotor to the stator frame of reference over the interface, and the rotating side is moved at each time step, see for instance Stridh & Eriksson (2005). The number of blades and vanes are important factors in noise generation, and it is thus important to keep this ratio in any aeroacoustic computation. In a modern high BPR engine, the number of blades and vanes in the fan stage is seldom the same, and standard periodic boundary conditions and a standard sliding grid interface can thus not be used with only one blade and one vane in each domain. Take as an example a fan stage with eight rotor blades and 12 stator vanes. Let the spinning lobe pattern in figure 2.2 be the first harmonic of the rotor wakes. It will spin at the same speed as the rotor, and it needs to be preserved when it enters the stator domain. As shown in figure 2.2, one stator domain will not contain the entire wave length of the mode. The stator domain must contain three vanes, and the rotor domain needs to contain two blades in this example in order to make it possible to make aeroacoustic simulations with standard periodic b.c. and a standard sliding grid interface. If one of the numbers is a prime number, the only alternative in this standard fashion is to make a 360^o computation.

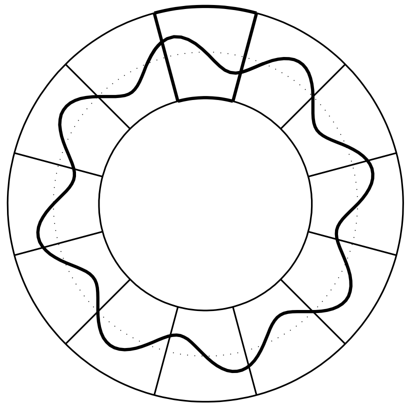

Figure 2.2: Spinning lobed pattern inside a duct with circumferential mode number m=8, divided into 12 domains

A full 360^o computation is of course very expensive. A way to get around this is to utilize the chorochronic periodicity, also known as the shape correction method (Gerolymos *et al.*, 2002; Li & He, 2001, 2002; Lebrun & Favre, 2004; Schnell, 2004). This is a time accurate method, and the time history at the periodic boundaries is sampled and saved and then time lagged. The interface between the rotating and the stationary domain utilizes eq. (1.1) to evaluate which circumferential modes should be passed over to the other domain. This tool is mainly used for solving the deterministic interactions (Papers I, II, IV, V) but it has also been used for simulations of turbulent fluctuations in a rotor wake as they impinge on stators (Paper III). This method is unstable since there is a delay between the time at which the information is sampled at the periodic boundaries and when it is used at the other side, because of the time lag. More details on the chorochronic method and how it can be made stable will be given in the next section (2.2.1).

There are also frequency domain linearized Navier-Stokes equations (LNSE) solvers that can solve for the rotor wake impingement on the stators, but not fully coupled. The time lag is then replaced by a phase shift in the frequency domain, and all perturbations on top of a mean flow solution are assumed to be linear. This is not a valid assumption for pressure waves with large amplitude but can still be an effective tool for predicting tonal noise from wake impingement on stators. An existing linearized solver that has been validated against independent data is used as a reference in Paper I and Paper II. For more details on this solver, see Baralon *et al.* (2005).

Another method is the time inclining technique, where the equations are changed so that the computational domain is inclined in time when moving in the circumferential direction. In this way there is no need to make a time shift over the periodic boundary, since the time shift is done gradually inside the domain (e.g. Giles, 1988*a*). The main drawbacks of this method are that the time incline can not be too steep because of stability problems and that the viscous terms are not treated correctly.

The harmonic balance technique can also be used for solving nonlinear unsteady deterministic rotor-stator interactions, see for instance Hall *et al.* (2002); Gopinath *et al.* (2007). The solver then solves for a discrete number of time levels over a period that is used to represent the harmonic content in the flow. This method requires more memory since a copy of the conservative variables has to be saved for each time level. However, the time history at the periodic boundaries is available without any delay which is an advantage of this method compared to the chorochronic time accurate method. The harmonic balance technique is used in Paper V and is described in more detail in section 2.4.

2.2.1 Chorochronic Periodicity

Chorochronic periodicity occurs when two blade rows with different blade count and different angular velocities interact. All blades in a blade row experience the same periodic flow but at different times. The name refers to a space (choros) and time (chronos) periodicity (Gerolymos *et al.*, 2002). Boundary conditions that utilize this periodicity are also given the prefix chorochronic, such as chorochronic periodic b. c. and chorochronic rotor-stator interface. The unsteady interacting flow in two blade rows with arbitrary blade counts can then be analyzed in a single-passage computation, i.e. a one blade per blade row computation.

The idea of using chorochronic periodicity to simplify blade row interaction computations is not new and there are many different methodologies for how to do it. The information have to be time lagged at the periodic boundaries before it is used on the other side. One way of doing this is to save information at the periodic boundaries for each time step directly and later use it at the other side, i.e. "direct store", described by e.g. Erdos *et al.* (1977); Koya & Kotake (1985). The method used in this thesis is to save the information at the periodic boundaries in finite Fourier series and evaluate them on the other side at a different time. This simplifies the storing of information, and the Fourier series can be continuously updated. This is known as a chorochronic method or a shape correction method and has been used for different blade row interaction studies, see for instance Gerolymos *et al.* (2002); Li & He (2001, 2002); Lebrun & Favre (2004); Schnell (2004).

The chorochronic periodic boundary condition has been shown to be unstable unless sufficient numerical damping is introduced, e.g. Li & He (2001, 2002); Schnell (2004). A good way to ensure that enough damping is introduced is to adopt temporal damping, and not introduce any extra spatial dissipation, as for example done by Schnell (2004), that uses some kind of filter on the Fourier coefficients. It is unclear exactly what the other authors that have used time lagged boundary conditions have done, but the numerical scheme itself might have had enough dissipation in some cases. A method that introduces extra spatial dissipation was used in Paper I, and it was shown not to be suitable for aeroacoustic calculations. Another method that damps out non-periodic flow close to the boundaries was used in Papers II-V and it gave good results for rotor-wake/stator interaction cases.

The Fourier coefficients are updated using a moving average technique similar to the one used by Gerolymos *et al.* (2002). The averaging algorithm can be derived from the definition of how a Fourier coefficient is calculated by integration over one period. In the stator blade row, that is:

$$\Phi_n = \frac{1}{T}\int_{t-T}^{t} Q(t')e^{-i\omega_n t'}dt' \tag{2.26}$$

where Φ_n is the n^{th} harmonic Fourier coefficients to the state vector, Q. The fundamental period, T, is the inverse of the BPF and it is calculated from the difference in angular velocity between the two blade rows and the number of blades in the rotor frame of reference as

$$T = \frac{2\pi}{N_{b,rotor}|\Omega_{rotor} - \Omega_{stator}|} \tag{2.27}$$

The angular frequency, ω_n, of each harmonic is calculated as

$$\omega_n = nN_{b,rotor}\Big(\Omega_{rotor} - \Omega_{stator}\Big) \tag{2.28}$$

The time derivatives of Fourier coefficients can be calculated from the integration bounds of eq. (2.26).

$$\frac{d\Phi_n}{dt} = \frac{1}{T}\Big[Q(t)e^{-i\omega_n t} - Q(t-T)e^{-i\omega_n(t-T)}\Big] \tag{2.29}$$

The state of the flow one period back in time can be approximated by evaluating the Fourier series as

$$Q(t-T) \approx \widehat{Q}(t) = \sum_n \Phi_n e^{i\omega_n t} \tag{2.30}$$

This can be used to find an approximate value of the Fourier coefficient derivative:

$$\frac{d\Phi_n}{dt} = \frac{1}{T}\Big[Q(t) - \sum_l \Phi_l e^{i\omega_l t}\Big]e^{-i\omega_n t} \tag{2.31}$$

The method described above is used in the area close to the periodic boundary in order to get a Fourier representation of the flow. The coefficients are evaluated at a different time to obtain the time lagged state that corresponds to the state on the other side of the periodic boundary. In Papers II-V, the Fourier coefficients are also used to damp out non-periodic flow phenomena that will contaminate the flow and eventually make the solution diverge if nothing else is done to handle it. The Fourier coefficients are then evaluated again, at the current time in the area where the sampling occurred, and compared to the state there in order to calculate a temporal damping term. The damping term is added to the state vector derivative as a source term as follows:

$$\frac{dQ}{dt} = \cdots - \epsilon\Big[Q(t) - \widehat{Q}(t)\Big] \tag{2.32}$$

The optimal value of the damping factor, ϵ, depends on the specific case. If the value is too low, there will be unphysical behavior close to the boundary, and pressure modes that should not be there will start to form and eventually make the solution diverge. There can be unphysical behavior for a little lower than an optimum value but the computation might still be stable and, if the value is too high, the convergence time to reach a periodic solution increases to almost infinity. The optimum might be to start with a low value and then gradually increase it, since it takes some time for the unphysical pressure modes to grow to an unhealthy size. The convective information in a wake, i.e. entropy and vorticity, is then allowed to be sampled without being damped out at the beginning of the simulation and, in the later stage, the pressure is allowed to adjust to the wake impingement with enough damping and prevent excitation of unphysical behavior.

2.2.2 Chorochronic Buffer Zone

In Paper III, a method based on hybrid RANS/LES and chorochronic buffer zones is used to obtain the low to medium frequency broadband noise from the rotor wake impingement on stators. The chorochronic buffer zone is a combination of a time lagged periodic boundary condition and a temporally damped region in the vicinity of it. The temporal damping in the buffer region is the same as the damping that is used to make the periodic b.c. with time lag stable (eq. 2.32), but here the damping is used in a larger region. Figure 2.3 shows a schematic of a computational domain for a hybrid RANS/LES calculation with chorochronic buffer zones.

The rotor is omitted in this type of calculation, but the rotor wake is specified at the inlet to the stator domain as an unsteady boundary condition. Isotropic synthetic fluctuations are added to the inlet boundary condition to trigger the equations into turbulent mode. The stator domain consists of three stator vanes to allow for some turbulent variations in the flow without too much influence from the periodic boundaries with buffer zones. The chorochronic buffer zones filter the flow from stochastic fluctuations, and the periodic boundary condition with time lag transfers the deterministic periodic variations in the flow to the other side. The pressure fluctuations on the center vane are sampled and used as a source for noise evaluation. Section 2.7 explains

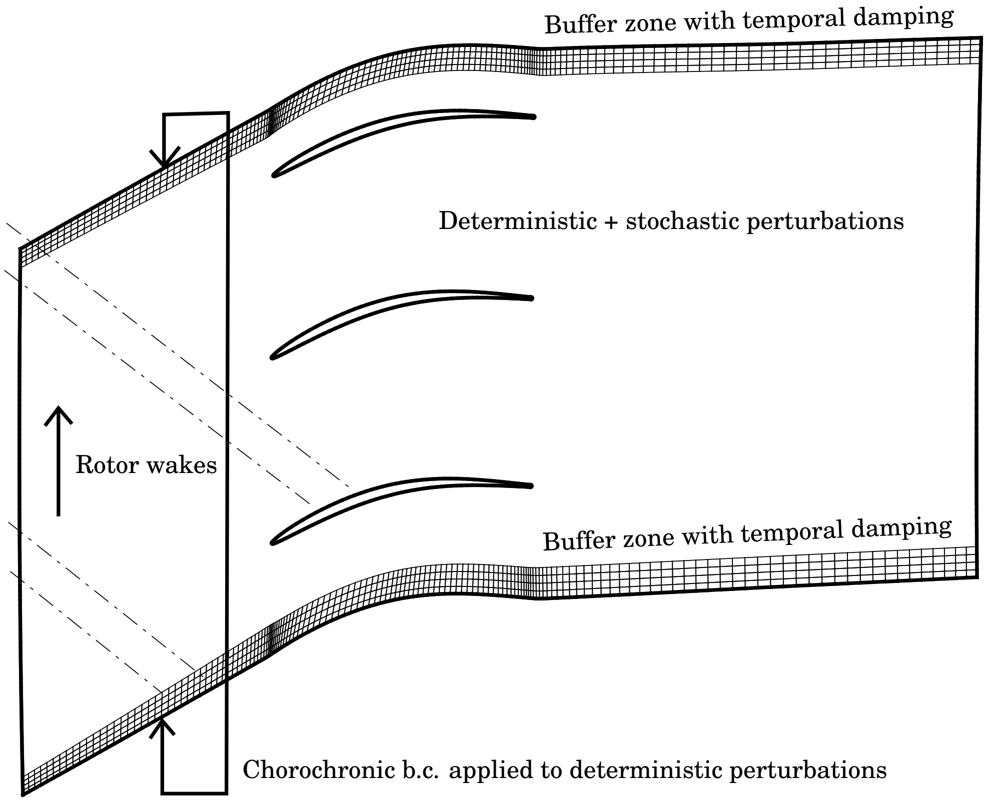

Figure 2.3: Schematic of a computational domain for a hybrid RANS/LES calculation with chorochronic buffer zones

how this works.

2.2.3 Chorochronic Rotor-Stator Interface

In Papers IV and V, a general Fourier-based interface that analyzes the modal content in the flow according to eq. (1.1) was used which is similar to the technique used by Gerolymos *et al.* (2002). A flow variation in the circumferential direction that is stationary in one frame of reference, with an angular velocity of Ω_1, will be unsteady in another frame of reference, with an angular velocity of $\Omega_2 \neq \Omega_1$. The modes that are passed on to the other frame of reference will therefore be shifted in frequency. The following theory holds for any pair of rotating blade rows but, for reasons of clarity, the two domains are labeled rotor and stator in the derivation.

The spinning interaction modes, $m_{n,k}$, are calculated from the theory of Tyler & Sofrin (1962).

$$m_{n,k} = nN_{b,rotor} + kN_{b,stator} \tag{2.33}$$

The angular frequencies of the modes in the stator frame of reference depend only on the rotor harmonics, n, and are calculated as

$$\omega_n = nN_{b,rotor}\Big(\Omega_{rotor} - \Omega_{stator}\Big) \tag{2.34}$$

The fundamental period should be a positive value and is calculated in the stator frame of reference as

$$T_{rotor} = \frac{2\pi}{N_{b,rotor}|\Omega_{rotor} - \Omega_{stator}|} \tag{2.35}$$

The angular frequencies and the fundamental period of the modes in the rotor frame of reference are calculated by eq. (2.36-2.37), i.e. the frequency depends only on the stator harmonics, k, and the stator BPF.

$$\omega_k = kN_{b,stator}\Big(\Omega_{stator} - \Omega_{rotor}\Big) \tag{2.36}$$

$$T_{stator} = \frac{2\pi}{N_{b,stator}|\Omega_{stator} - \Omega_{rotor}|} \tag{2.37}$$

Time Fourier series representations of the flow in the area close to the interface are updated as in eq. (2.31), but for the primitive variables, q, in a cylindrical coordinate system:

$$\frac{d\phi_n^{stator}(\theta)}{dt} = \frac{1}{T_{rotor}}\Big[q(t,\theta) - \sum_l \phi_l^{stator}(\theta)e^{i\omega_l t}\Big]e^{-i\omega_n t} \tag{2.38}$$

$$\frac{d\phi_k^{rotor}(\theta)}{dt} = \frac{1}{T_{stator}}\Big[q(t,\theta) - \sum_l \phi_l^{rotor}(\theta)e^{i\omega_l t}\Big]e^{-i\omega_k t} \tag{2.39}$$

where

$$q = \begin{bmatrix} \overline{\rho} \\ \tilde{u}_x \\ \tilde{u}_r \\ \tilde{u}_\theta \\ \overline{p} \\ \tilde{k} \\ \tilde{\varepsilon} \end{bmatrix} \tag{2.40}$$

Sampling is done on both sides of the interface to get a complete representation of the flow information in both time and space. The following derivation is made for a constant radius section of the interface, and the time and space Fourier coefficients of the modes, $m_{n,k}$, are calculated by integrating the time Fourier coefficients to each sector in the circumferential direction as

$$\phi_{n,k} = \frac{N_{b,stator}}{2\pi} \int_0^{\frac{2\pi}{N_{b,stator}}} \phi_n^{stator}(\theta) e^{im_{n,k}\theta} d\theta \tag{2.41}$$

$$\phi_{n,k} = \frac{N_{b,rotor}}{2\pi} \int_0^{\frac{2\pi}{N_{b,rotor}}} \phi_k^{rotor}(\theta) e^{im_{n,k}\theta} d\theta \tag{2.42}$$

These modes can now be passed on to any rotating frame of reference by a shift in frequency. The frequency according to eq. (2.34) is used in the stator frame of reference. The evaluation is made by a summation over all the Fourier modes:

$$\widehat{q}_{stator}(t,\theta) = \sum_n \sum_k \phi_{n,k} e^{i\omega_n t} e^{-im_{n,k}\theta} \tag{2.43}$$

The angular frequency according to eq. (2.36) should be used when this state is transferred to the rotor side of the interface:

$$\widehat{q}_{rotor}(t,\theta) = \sum_n \sum_k \phi_{n,k} e^{i\omega_k t} e^{-im_{n,k}\theta} \tag{2.44}$$

Note that it is assumed in eqns. (2.43-2.44) that both positive and negative frequencies are used, i.e.

$$\begin{aligned} n &= ... - 1, 0, 1... \\ k &= ... - 1, 0, 1... \end{aligned} \tag{2.45}$$

Some simplifications can be made by only calculating coefficients for positive frequencies and then using the complex conjugates to obtain the full matrix of Fourier coefficients to the modes:

$$\phi_{-n,-k} = \phi_{n,k}^* \tag{2.46}$$

2.3 Inflow/Outflow Boundary Conditions

Inflow and outflow boundaries are needed in CFD simulations when the computational domain is smaller than the physical flow domain. This is often a necessity since it is usually not possible to always model everything at the same time. Further, the computational domain should be made as small as possible to make the most efficient use of the CFD tool, and the flow path will be cut in between stages in a turbomachine for instance when different components are analyzed separately. Typical subsonic boundary conditions for the inviscid part of compressible flow are to specify total pressure, total temperature and a direction vector at an inlet (normal velocity component is extrapolated) and static pressure at an outlet (density and velocity vector are extrapolated). These examples are straightforward to implement in the code and easy to understand since these properties can often be measured easily. Problems arise when unsteady simulations are desired, such as aeroacoustics, because a sound wave that propagates towards a pressure outlet boundary condition will be 100% reflected. This is an artificial reflection and it will contaminate the flow. Further, if a vorticity wave exits through a pressure outlet, acoustic waves will be created that also contaminate the solution. Acoustic waves may also reach the inlet boundary and, even though the reflection in a total pressure inlet boundary condition is not 100%, it is still too much. Much work has been done on making inflow and outflow boundaries absorbing, and e.g. Colonius (2004) wrote a substantial review of the subject. There are mainly two different approaches for making boundaries absorbing that are used either separately or in combination. The first one is to artificially treat the boundary so that it absorbs waves. The second is to have a damping zone in the vicinity of the boundary that artificially damps unsteady waves, i.e. a buffer layer.

All boundary conditions in the code are specified by a ghost cell technique, i.e. two imaginary cell layers outside of the boundary are created and the state is specified there to obtain the desired function at the boundary. The same scheme that is used in the interior can then be used over the boundary as well.

2.3.1 Absorbing Boundary Conditions

Early work with absorbing boundaries was done by Engquist & Majda (1977) and Hedstrom (1979). Giles (1988*b*, 1990) later made significant contributions. The inviscid part of the Navier-Stokes equations, i.e. the Euler equations, is essential in constructing absorbing boundary conditions, and the equations are linearized so that perturbations on top of a reference state are considered. Different types of boundary conditions are obtained by assuming different flow behaviors and a more general boundary condition usually means greater complexity. Also, if for instance duct modes are considered, a perfectly absorbing boundary condition needs to know which modes approach the boundary, and the flow needs to be analyzed at the entire boundary to be able to specify the condition at one point on the boundary. This means that the boundary condition is nonlocal in contrast to more simple but perhaps not perfectly absorbing local boundary conditions that can be specified by local information.

Two-dimensional

A 2D absorbing boundary condition for 2D nonlinear flow was developed by Chassaing & Gerolymos (2007). This approach has been extended for 3D flow inside a duct to make a boundary condition that absorbs axial and circumferential characteristics. It was used in Papers IV and V and is derived from the assumption of flow inside a thin shell annulus at radius R where radial variations are neglected and the reference state is assumed to be:

$$\begin{cases} \rho &= \rho_{ref} \\ u_x &= u_x^{ref} \\ u_r &= 0 \\ u_\theta &= u_\theta^{ref} \\ p &= p_{ref} \end{cases} \tag{2.47}$$

The fluctuating component is assumed to vary as

$$\begin{cases} \rho' &= \rho'(x,\theta,t) \\ u'_x &= u'_x(x,\theta,t) \\ u'_r &= u'_r(x,\theta,t) \\ u'_\theta &= u'_\theta(x,\theta,t) \\ p' &= p'(x,\theta,t) \end{cases} \tag{2.48}$$

The linearized Euler equations in a cylindrical coordinate system can then be written as

$$\begin{cases} \frac{\partial \rho'}{\partial t} + u_x^{ref}\frac{\partial \rho'}{\partial x} + u_\theta^{ref}\frac{1}{R}\frac{\partial \rho'}{\partial \theta} + \rho_{ref}\left[\frac{\partial u'_x}{\partial x} + \frac{\partial u'_\theta}{\partial \theta}\right] = -\rho_{ref}\frac{u'_r}{R} \\ \frac{\partial u'_x}{\partial t} + u_x^{ref}\frac{\partial u'_x}{\partial x} + u_\theta^{ref}\frac{1}{R}\frac{\partial u'_x}{\partial \theta} + \frac{1}{\rho_{ref}}\frac{\partial p'}{\partial x} = 0 \\ \frac{\partial u'_r}{\partial t} + u_x^{ref}\frac{\partial u'_r}{\partial x} + u_\theta^{ref}\frac{1}{R}\frac{\partial u'_r}{\partial \theta} = \frac{2u_\theta^{ref}}{R}u'_\theta \\ \frac{\partial u'_\theta}{\partial t} + u_x^{ref}\frac{\partial u'_\theta}{\partial x} + u_\theta^{ref}\frac{1}{R}\frac{\partial u'_\theta}{\partial \theta} + \frac{1}{\rho_{ref}}\frac{1}{R}\frac{\partial p'}{\partial \theta} = -\frac{u_\theta^{ref}}{R}u'_r \\ \frac{\partial p'}{\partial t} + u_x^{ref}\frac{\partial p'}{\partial x} + u_\theta^{ref}\frac{1}{R}\frac{\partial p'}{\partial \theta} + \rho_{ref}c_{ref}^2\left[\frac{\partial u'_x}{\partial x} + \frac{\partial u'_\theta}{\partial \theta}\right] = -\frac{\rho_{ref}c_{ref}^2}{R}u'_r \end{cases} \tag{2.49}$$

If the lower-order terms are neglected, the equations reduce to

$$\frac{\partial q'}{\partial t} + A_{ref}\frac{\partial q'}{\partial x} + C_{ref}\frac{1}{R}\frac{\partial q'}{\partial \theta} = 0 \tag{2.50}$$

where

$$q' = \begin{bmatrix} \rho' \\ u'_x \\ u'_r \\ u'_\theta \\ p' \end{bmatrix} \tag{2.51}$$

and

$$A_{ref} = \begin{bmatrix} u_x^{ref} & \rho_{ref} & 0 & 0 & 0 \\ 0 & u_x^{ref} & 0 & 0 & 1/\rho_{ref} \\ 0 & 0 & u_x^{ref} & 0 & 0 \\ 0 & 0 & 0 & u_x^{ref} & 0 \\ 0 & \rho_{ref} c_{ref}^2 & 0 & 0 & u_x^{ref} \end{bmatrix} \tag{2.52}$$

and

$$C_{ref} = \begin{bmatrix} u_\theta^{ref} & 0 & 0 & \rho_{ref} & 0 \\ 0 & u_\theta^{ref} & 0 & 0 & 0 \\ 0 & 0 & u_\theta^{ref} & 0 & 0 \\ 0 & 0 & 0 & u_\theta^{ref} & 1/\rho_{ref} \\ 0 & 0 & 0 & \rho_{ref} c_{ref}^2 & u_\theta^{ref} \end{bmatrix} \tag{2.53}$$

The flow inside the duct is assumed to contain spinning modes with no radial variations, and solutions of the form

$$q' = \phi \, e^{i\omega t} e^{-im\theta} e^{ik_x x} \tag{2.54}$$

can be assumed. Combining this assumption with eq. (2.50) gives:

$$i\omega\phi \; - \; i\frac{m}{R} C_{ref}\phi \; - \; ik_x A_{ref}\phi \; = \; 0 \tag{2.55}$$

that can be rewritten as

$$\left[k_x A_{ref} \; + \; \frac{m}{R} C_{ref} \; - \; \omega I \right] \phi \; = \; 0 \tag{2.56}$$

which is equal to

$$\begin{bmatrix} (k_x u_x^{ref} + \frac{m}{R} u_\theta^{ref} - \omega) & k_x \rho_{ref} & 0 & \frac{m}{R}\rho_{ref} & 0 \\ 0 & (k_x u_x^{ref} + \frac{m}{R} u_\theta^{ref} - \omega) & 0 & 0 & \frac{k_x}{\rho_{ref}} \\ 0 & 0 & (k_x u_x^{ref} + \frac{m}{R} u_\theta^{ref} - \omega) & 0 & 0 \\ 0 & 0 & 0 & (k_x u_x^{ref} + \frac{m}{R} u_\theta^{ref} - \omega) & \frac{m}{R\rho_{ref}} \\ 0 & k_x \rho_{ref} c_{ref}^2 & 0 & \frac{m}{R}\rho_{ref} c_{ref}^2 & (k_x u_x^{ref} + \frac{m}{R} u_\theta^{ref} - \omega) \end{bmatrix} \phi \; = \; 0 \tag{2.57}$$

Setting the determinant of the matrix equal to zero gives two equations; The first is

$$\left(\omega - k_x u_x^{ref} - \frac{m}{R} u_\theta^{ref}\right)^3 = 0 \tag{2.58}$$

The second is

$$\left(\omega - k_x u_x^{ref} - \frac{m}{R} u_\theta^{ref}\right)^2 = c_{ref}^2 \left(k_x^2 + \frac{m^2}{R^2}\right) \tag{2.59}$$

The first equation has three roots and the latter has two roots. Both ω and m are known if the interaction modes of a rotor stator computation are considered. The equations (2.58) and (2.59) can be solved for k_x with a fixed ω and a fixed m and roots 1,2 and 3 are:

$$k_{x,1} = k_{x,2} = k_{x,3} = \frac{\omega - \frac{m}{R} u_\theta^{ref}}{u_x^{ref}} \tag{2.60}$$

These roots are always real numbers, and they correspond to the wave numbers of the characteristic variables, i.e. the entropy wave and the two vorticity waves. The wave numbers for the acoustic waves are roots 4 and 5 from the equation:

$$k_x^2 \;+\; \frac{2u_x^{ref}\left(\omega - \frac{m}{R} u_\theta^{ref}\right)}{\left(c_{ref}^2 - u_x^{ref\,2}\right)} k_x \;+\; \frac{\left(c_{ref}^2 - u_\theta^{ref\,2}\right)\frac{m^2}{R^2} + 2u_\theta^{ref}\omega\frac{m}{R} - \omega^2}{\left(c_{ref}^2 - u_x^{ref\,2}\right)} \;=\; 0 \tag{2.61}$$

These roots are either real or complex and they correspond to either cut-on or cut-off acoustic modes. The transformation matrix, $\mathcal{T}$, that transforms the characteristic variables to the primitive as

$$q' = \mathcal{T} W \tag{2.62}$$

and the primitive to the characteristic as

$$W = \mathcal{T}^{-1} q' \tag{2.63}$$

is also needed. The columns of $\mathcal{T}$ are the eigenvectors of the characteristic variables and can be written as

$$\mathcal{T} \;=\; \begin{bmatrix} 1 & 0 & 0 & \frac{\rho_{ref}}{c_{ref}} & \frac{\rho_{ref}}{c_{ref}} \\ 0 & \frac{-\frac{m}{R}}{\sqrt{k_{x,2}^2+\frac{m^2}{R^2}}} & 0 & \frac{-c_{ref}k_{x,4}}{k_{x,4}u_x^{ref}+\frac{m}{R}u_\theta^{ref}-\omega} & \frac{-c_{ref}k_{x,5}}{k_{x,5}u_x^{ref}+\frac{m}{R}u_\theta^{ref}-\omega} \\ 0 & 0 & 1 & 0 & 0 \\ 0 & \frac{k_{x,2}}{\sqrt{k_{x,2}^2+\frac{m^2}{R^2}}} & 0 & \frac{-c_{ref}\frac{m}{R}}{k_{x,4}u_x^{ref}+\frac{m}{R}u_\theta^{ref}-\omega} & \frac{-c_{ref}\frac{m}{R}}{k_{x,5}u_x^{ref}+\frac{m}{R}u_\theta^{ref}-\omega} \\ 0 & 0 & 0 & \rho_{ref}c_{ref} & \rho_{ref}c_{ref} \end{bmatrix} \tag{2.64}$$

and its inverse is given by:

$$\mathcal{T}^{-1} = \begin{bmatrix} 1 & 0 & 0 & 0 & \frac{-1}{c_{ref}^2} \\ 0 & \frac{-\frac{m}{R}}{\sqrt{k_{x,2}^2+\frac{m^2}{R^2}}} & 0 & \frac{k_{x,2}}{\sqrt{k_{x,2}^2+\frac{m^2}{R^2}}} & \frac{-\frac{m}{R}}{\rho_{ref}u_x^{ref}\sqrt{k_{x,2}^2u_x^{ref}+\frac{m^2}{R^2}}} \\ 0 & 0 & 1 & 0 & 0 \\ 0 & \frac{k_{x,2}F_4F_5}{c_{ref}F_{45}F_2} & 0 & \frac{\frac{m}{R}F_4F_5}{c_{ref}F_{45}F_2} & \frac{\left(k_{x,2}k_{x,5}+\frac{m^2}{R^2}\right)F_4}{\rho_{ref}c_{ref}F_{45}F_2} \\ 0 & \frac{-k_{x,2}F_4F_5}{c_{ref}F_{45}F_2} & 0 & \frac{-\frac{m}{R}F_4F_5}{c_{ref}F_{45}F_2} & \frac{-\left(k_{x,2}k_{x,4}+\frac{m^2}{R^2}\right)F_5}{\rho_{ref}c_{ref}F_{45}F_2} \end{bmatrix} \tag{2.65}$$

where

$$\begin{cases} F_2 = \frac{m^2}{R^2}u_x^{ref} - k_{x,2}\frac{m}{R}u_\theta^{ref} + k_{x,2}\omega = \left(k_{x,2}^2 + \frac{m^2}{R^2}\right)u_x^{ref} \\ F_4 = k_{x,4}u_x^{ref} + \frac{m}{R}u_\theta^{ref} - \omega \\ F_5 = k_{x,5}u_x^{ref} + \frac{m}{R}u_\theta^{ref} - \omega \\ F_{45} = k_{x,4} - k_{x,5} \end{cases} \tag{2.66}$$

These matrices are used to extrapolate the waves that leave the domain at the inflow or outflow boundary. The group velocity, $\partial\omega/\partial k$, is used to determine the direction in which the information goes; it can be calculated from equations (2.60) and (2.61). The group velocity for roots 1,2 and 3 is

$$\frac{\partial\omega}{\partial k_{x,1}} = \frac{\partial\omega}{\partial k_{x,2}} = \frac{\partial\omega}{\partial k_{x,3}} = u_x^{ref} \tag{2.67}$$

and the group velocities for roots 4 and 5 are:

$$\begin{cases} \frac{\partial\omega}{\partial k_{x,4}} = u_x^{ref} + \frac{c_{ref}^2 k_{x,4}}{\omega - u_x^{ref}k_{x,4} - \frac{m}{R}u_\theta^{ref}} \\ \frac{\partial\omega}{\partial k_{x,5}} = u_x^{ref} + \frac{c_{ref}^2 k_{x,5}}{\omega - u_x^{ref}k_{x,5} - \frac{m}{R}u_\theta^{ref}} \end{cases} \tag{2.68}$$

The sign of the imaginary part of the wave number is used instead of the group velocity if an acoustic mode is cut-off, i.e. a check on the direction of the damping.

The machinery behind this boundary condition is very similar to the machinery behind the chorochronic rotor-stator interface described in section 2.2.3. The state close to the boundary is sampled into Fourier coefficients and the time and space Fourier coefficients for each mode are calculated. These coefficients are then decomposed into the characteristic variables according to the above recipe, and the outgoing characteristics are extrapolated to the ghost cells outside the boundary. As pointed out in Papers IV and V, problems arise when a cut-on mode is close to cut-off and vice versa. A real 3D duct mode is either cut-on or cut-off but, according to the 2D characteristic analysis, a circumferential mode can be cut-on at a large radius and cut-off close to the hub. The 2D analysis fails at the radial location where the transition occurs. One solution to the problem is to exclude the modes that are cut-off or close to cut-off from being extrapolated to ghost cells, as was done in Paper V.

One-dimensional

If the mode number is equal to zero, transformation matrices $\mathcal{T}$ and $\mathcal{T}^{-1}$ reduce to

$$\mathcal{T} = \begin{bmatrix} 1 & 0 & 0 & \frac{\rho_{ref}}{c_{ref}} & \frac{\rho_{ref}}{c_{ref}} \\ 0 & 0 & 0 & 1 & -1 \\ 0 & 0 & 1 & 0 & 0 \\ 0 & 1 & 0 & 0 & 0 \\ 0 & 0 & 0 & \rho_{ref}c_{ref} & \rho_{ref}c_{ref} \end{bmatrix} \tag{2.69}$$

and

$$\mathcal{T}^{-1} = \begin{bmatrix} 1 & 0 & 0 & 0 & \frac{-1}{c_{ref}^2} \\ 0 & 0 & 0 & 1 & 0 \\ 0 & 0 & 1 & 0 & 0 \\ 0 & \frac{1}{2} & 0 & 0 & \frac{1}{2\rho_{ref}c_{ref}} \\ 0 & \frac{-1}{2} & 0 & 0 & \frac{1}{2\rho_{ref}c_{ref}} \end{bmatrix} \tag{2.70}$$

and the group velocities becomes:

$$\begin{cases} \frac{\partial \omega}{\partial k_{x,1}} = \frac{\partial \omega}{\partial k_{x,2}} = \frac{\partial \omega}{\partial k_{x,3}} = u_x^{ref} \\ \frac{\partial \omega}{\partial k_{x,4}} = u_x^{ref} + c_{ref} \\ \frac{\partial \omega}{\partial k_{x,5}} = u_x^{ref} - c_{ref} \end{cases} \tag{2.71}$$

This is a 1D absorbing boundary condition in the axial direction, and it can be made local, i.e. not dependent on Fourier sampling and mode decomposition, by assuming that the reference state is the actual instantaneous state at each point on the boundary. This type of boundary condition is usually generalized to absorb waves normal to the boundary and has as such been used in all papers on which this thesis is based.

2.3.2 Buffer Layer

A region close to an inflow or an outflow boundary may be artificially treated to damp unsteady fluctuations. This can improve the performance of an absorbing boundary condition or can replace it when used together with a more simple boundary condition. Buffer layers have been called by various names in the literature, e.g. sponge layer or exit zone, but the main idea is the same, namely to add an additional term to the governing equations that damps unsteady flow. This particular method was first proposed by Colonius *et al.* (1993) and has later been analyzed by e.g. Richards *et al.* (2004) and Bodony (2006). The additional term can be written as

$$\frac{dQ}{dt} = \cdots - \epsilon\left(x\right)\left[Q - \langle Q\rangle\right] \tag{2.72}$$

where ϵ is a damping factor and $\langle\cdot\rangle$ implies a time average. Both constant and varying values of the damping factor have been tested. A function based on an arcus tangent has been used in the buffer layers with a varying value of ϵ. It can be written as

$$\frac{\epsilon\left(x\right)}{\epsilon_{max}} = \frac{1-\frac{\epsilon_{min}}{\epsilon_{max}}}{2\;atan\left(\pi s\right)}\;atan\left(2\pi s\frac{\left(x-x_{start}\right)}{\left(x_{b.c.}-x_{start}\right)} - \pi s\right) + \frac{1}{2}\left(1+\frac{\epsilon_{min}}{\epsilon_{max}}\right) \tag{2.73}$$

where ϵ_{max} and ϵ_{min} are the maximum and minimum damping respectively, s is a shape parameter, x_{start} is the axial position at which the buffer layer starts and $x_{b.c.}$ is the axial position of the inflow or outflow boundary. The reason for using this kind of function is to avoid high gradients at the beginning and at the end of the buffer layer in order to avoid reflections. Figure 2.4 shows this function for three values of the shape parameter; it can be seen that high values of s give a step-like function while low values give a linear-like function.

The time average, $\langle Q\rangle$, is calculated by using a low-pass filter that continuously updates a reference state, i.e. the time average of the flow. The reference state is updated every time step as

$$\langle Q\rangle^{p} = b\,\langle Q\rangle^{p-1} + \left(1-b\right)Q^{p} \tag{2.74}$$

where b is a constant that determines the cutoff frequency of the filter. This constant can be set to:

$$b \;=\; 1 - \omega_c\,\Delta t \tag{2.75}$$

where ω_c is the cutoff frequency and Δt is the time step size. An approximately similar expression is

$$b \;\approx\; 1 - \frac{1}{N_{ave}} \tag{2.76}$$

where N_{ave} is the number of time steps over which the averaging should be made.

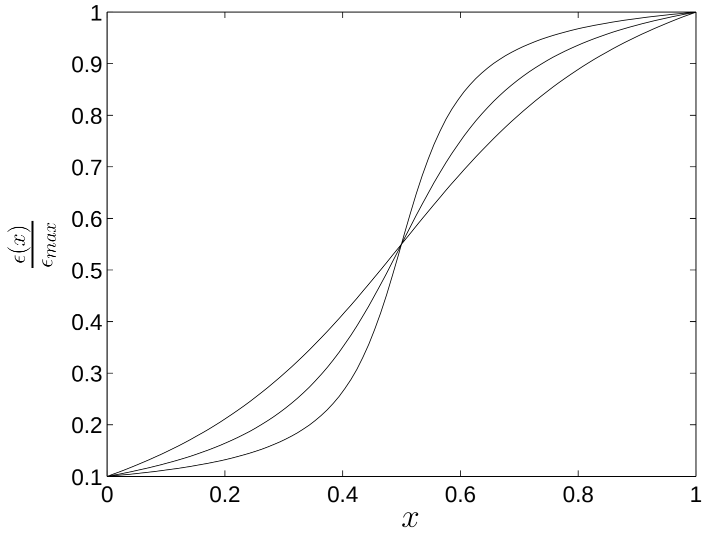

Figure 2.4: Damping function for three values of s; $s = 0.5, 1, 2$. Maximum damping $\epsilon_{max} = 1$, minimum damping $\epsilon_{min} = 0.1$, axial start position $x_{start} = 0$ and position of the boundary $x_{b.c.} = 1$. High values of s give a step-like function and low values a linear-like function.

The value of ϵ can be estimated by the residence time of an unsteady flow perturbation inside the buffer layer as it propagates towards the boundary as

$$\epsilon \approx \frac{1}{\tau} \tag{2.77}$$

where τ is the residence time. The value of ϵ_{max} for the cases with a varying damping factor has been set to about two times that of eq. (2.77).

Grid stretching was used in Paper VI as a method for dissipating unsteady waves. This is a simple approach that does not require any additional terms in the governing equations. A drawback of this approach is that waves with different length scales are not equally penalized.

2.4 Harmonic Balance Technique

The harmonic balance technique can be used to solve nonlinear time periodic flows. This is a time spectral method and is used in Paper V and compared to the time accurate method with chorochronic boundary conditions. A summary of what can be found in literature, e.g. Hall *et al.* (2002); Gopinath *et al.* (2007), on the derivation of this technique is given in the following paragraph.

The period of the unsteady flow must be known and the solution will be approximated by a finite Fourier series with N_h number of harmonics.

$$Q(t) \approx \sum_{n=-N_h}^{N_h} \Phi_n e^{i\omega_n t} \tag{2.78}$$

The time derivative can be calculated from the Fourier coefficients as

$$\frac{\partial Q}{\partial t} = \sum_{n=-N_h}^{N_h} i\omega_n \phi_n e^{i\omega_n t} \tag{2.79}$$

The time period is divided into a discreet number of time levels as

$$N_{tl} = 2N_h + 1 \tag{2.80}$$

A new state vector, Q^*, with the solution at each time level is constructed.

$$Q^* = \left[Q_{t_1},\ Q_{t_2},\ \dots\ , Q_{t_{N_{tl}}} \right] \tag{2.81}$$

The Fourier coefficients to the solution can easily be obtained from the time levels of the state vector, Q^*.

$$\phi_n = \frac{1}{N_{tl}} \sum_{l=1}^{N_{tl}} Q_{t_l} e^{-i\omega_n t_l} \tag{2.82}$$

An expression for the time derivative at any time, t, can be obtained by combining equations (2.79) and (2.82).

$$\frac{\partial Q}{\partial t} = \sum_{n=-N_h}^{N_h} i\omega_n \frac{1}{N_{tl}} \sum_{l=1}^{N_{tl}} Q_{t_l} e^{-i\omega_n t_l} e^{i\omega_n t} \tag{2.83}$$

Rearranging this equation gives

$$\frac{\partial Q}{\partial t} = \sum_{l=1}^{N_{tl}} Q_{t_l} \frac{1}{N_{tl}} \sum_{n=-N_h}^{N_h} i\omega_n e^{i\omega_n (t-t_l)} \tag{2.84}$$

The second summation in eq. (2.84) does not depend on the state vector and can be seen as coefficients in a linear combination of the time levels. The coefficients are defined as

$$D_{t_l}(t) = \frac{1}{N_{tl}} \sum_{n=-N_h}^{N_h} i\omega_n e^{i\omega_n (t-t_l)} \tag{2.85}$$

Using this, the time derivative can then be written as

$$\frac{\partial Q}{\partial t} = \sum_{l=1}^{N_{tl}} Q_{t_l}\, D_{t_l}\,(t) \tag{2.86}$$

The time derivative of the state vector, Q^*, can now be computed as

$$S^* = \frac{\partial Q^*}{\partial t} = \sum_{l=1}^{N_{tl}} \left[Q_{t_l}\, D_{t_l}\,(t_1)\,,\; Q_{t_l}\, D_{t_l}\,(t_2)\,,\; \dots\; , Q_{t_l}\, D_{t_l}\,(t_{N_{tl}})\right] \tag{2.87}$$

where the coefficients in eq. (2.85) are evaluated at the time levels of the state vector. A new governing equation for the state vector, Q^*, can be written as

$$\frac{\partial Q^*}{\partial \tau} + S^* + \frac{\partial \mathcal{F}_j^*}{\partial x_j} = \mathcal{H}^* \tag{2.88}$$

where the solution is updated by using a pseudo time, τ, and the true time derivative is treated as a source term, S^*. The fluxes, $\mathcal{F}_j^*$, and source terms, $\mathcal{H}^*$, are the same as in a standard URANS solver. They are evaluated at the time levels of the solution as

$$\mathcal{F}_j^* = \left[\mathcal{F}_j|_{t_1},\; \mathcal{F}_j|_{t_2},\; \dots\; , \mathcal{F}_j|_{t_{N_{tl}}}\right] \tag{2.89}$$

$$\mathcal{H}^* = \left[\mathcal{H}|_{t_1},\; \mathcal{H}|_{t_2},\; \dots\; , \mathcal{H}|_{t_{N_{tl}}}\right] \tag{2.90}$$

The coefficients in eq. (2.85) can be computed outside of the loop over each cell in the domain and the computational effort is negligible. The total time necessary to compute the time derivative source term is also small compared to the flux calculations. The computational time to reach convergence to a periodic solution can be reduced a great deal with this technique compared to standard time stepping methods. The main reason for this is that the same methods that are used to speed up convergence in steady state calculations, e.g. local time stepping, can be used with the harmonic balance technique. However, tests have shown that convergence is not always guaranteed, as discussed in Paper V, and it was a slow process in the cases that did converge. There was a slowly growing instability in one of the test cases that contaminated the solution after a while, and convergence was not reached. This instability was suppressed by the Newton-GMRES algorithm that was implemented in the solver after Paper V was published. The Newton-GMRES technique also reduced the time to reach convergence for the cases without instabilities and it is described in section 2.5.

There may also be truncation errors at the higher frequencies that are included in the spectral treatment. The solution to this has been to add a few extra frequencies to those that are of main interest.

The Fourier based boundary conditions, e.g. periodic with time lag and rotor-stator interface, do not need the sampling routine to update the Fourier coefficients when the harmonic balance technique is used since the entire period is available in the new state vector, Q^*. The Fourier coefficients at the boundaries are calculated directly from the state vector. The reference state in the buffer layer is also calculated directly from the state vector as a mean value of all time levels instead of using a low-pass filter as done when standard time stepping is used.

2.5 Newton-GMRES

The generalized minimal residual method (GMRES), proposed by Saad & Schultz (1986), is an iterative method for solving linear systems. The method is based on the Arnoldi process for constructing an orthogonal basis of Krylov subspaces and it was later combined with an inexact Newton method to form the Newton-GMRES method, that can be applied to nonlinear problems, by e.g. Brown & Saad (1994). One main advantage of this method is that the Jacobian matrix, J, is never needed explicitly, only J times a vector, v. The Newton-GMRES method can find a solution, x_*, to:

$$F(x) = 0 \tag{2.91}$$

where F is a nonlinear function and x is a vector field. The algorithm can be summarized by the following steps:

1. Choose an initial guess, x_0, and the number of Krylov vectors, m.
2. Arnoldi process:
   - Compute:
   $$r_0 = F(x_0) \tag{2.92}$$
   $$\beta = \|r_0\| \tag{2.93}$$
   - Define the first Krylov vector as
   $$v_1 = \frac{r_0}{\beta} \tag{2.94}$$
   - For $i = 1, m$ do:
     (a) Compute $w = F'(x_0)v_i$
     (b) For $j = 1, i$ do:
     $$h_{j,i} = \langle w, v_j \rangle \tag{2.95}$$
     $$w = w - h_{j,i}v_j \tag{2.96}$$
     where $\langle \cdot, \cdot \rangle$ denotes scalar product.

(c) Compute:

$$h_{i+1,i} = \|w\| \tag{2.97}$$

$$v_{i+1} = \frac{w}{h_{i+1,i}} \tag{2.98}$$

3. Define $\bar{H}_m$ to be the upper Hessenberg matrix with $(m+1) \times (m)$ elements and where the nonzero entries are the coefficients $h_{j,i}$ that are calculated in the Arnoldi process:

$$\bar{H}_m = \begin{bmatrix} h_{1,1} & h_{1,2} & \cdots & & h_{1,m} \\ h_{2,1} & h_{2,2} & & & \\ & h_{3,2} & & & \vdots \\ & & \ddots & & \\ \mathbf{0} & & & h_{m-1,m} & h_{m,m} \\ & & & & h_{m+1,m} \end{bmatrix} \tag{2.99}$$

Define $V_m \equiv [v_1, v_2, \dots, v_m]$.

- Find the vector y_m which minimizes:

$$\left\|\beta e_1 - \bar{H}_m y\right\| \tag{2.100}$$

where $e_1 = [1, 0, \dots, 0]^T$.

- Compute a new solution vector:

$$x_0 = x_0 + V_m y_m \tag{2.101}$$

4. Stop if x_0 is a good enough approximation to a root of (2.91), otherwise go back to 2.

This is how the Newton-GMRES method was implemented in this thesis. It is almost the same as how Brown & Saad (1994) describe it except that they have a varying number of Krylov vectors and a checking routine to indicate whether another vector should be added inside the Arnoldi process.

In the case of CFD applications, the Newton-GMRES method can for instance be used to find a stationary solution. If for example

$$\dot{x} = F(x) \tag{2.102}$$

eq. (2.91) gives the stationary solution. On the other hand, it is not practical to use $F(x)$ directly. It is better to use the time stepping, or pseudo time stepping, routines in the CFD code. If

$$x^{p+N} = G(x^p) \tag{2.103}$$

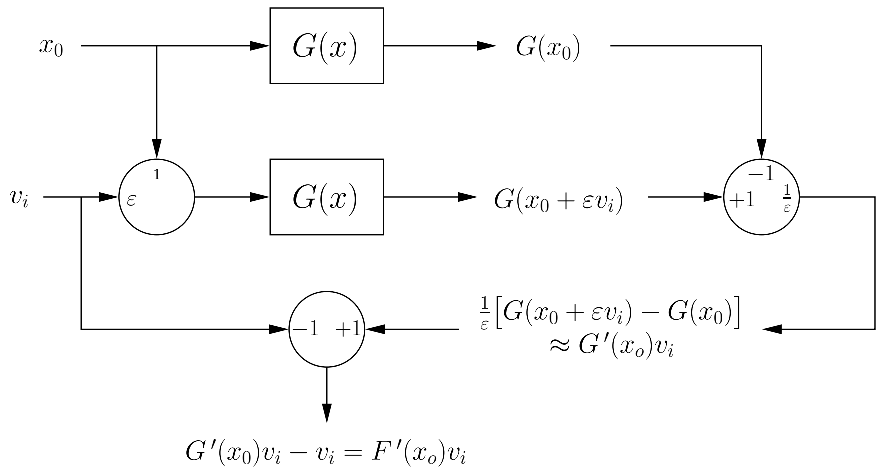

Figure 2.5: Process of finding the derivatives in the GMRES routine

where $x^p = x(t_p)$ and N is a number of time steps, then the stationary solution is obtained when $x^{p+N} = x^p = x$, i.e. when

$$G\left(x\right) = x \tag{2.104}$$

Vector x should contain all the degrees of freedom (DOF) of the problem and function F can be rewritten as

$$F\left(x\right) = G\left(x\right) - x \tag{2.105}$$

and r_0 is then calculated as

$$r_0 = G\left(x_0\right) - x_0 \tag{2.106}$$

The Arnoldi process also needs $F'(x_0)$ times a vector v_i. This can be calculated and approximated as

$$F'\left(x_0\right)v_i = G'\left(x_0\right)v_i - v_i \approx \frac{1}{\varepsilon}\Big[G\left(x_0+\varepsilon v_i\right) - G\left(x_0\right)\Big] - v_i \tag{2.107}$$

where ε is a small number. Figure 2.5 shows this equation as a flowchart.

The DOF for a 3D unsteady RANS computation with a two-equation turbulence model that is solved with the harmonic balance technique is $7 \times (number\ of\ cells) \times N_{tl}$. This is the dimension of vectors x, x_0, r_0, v_i, w and, as the number of Krylov vectors is increased, the Newton-GMRES algorithm requires more memory. The Krylov vectors are therefore stored on disk even though the number of vectors used in this thesis were not that many; three vectors give good performance.

The sum of $x_0 + \varepsilon v_i$ may sometimes result in negative values for the turbulence variables and should therefore be limited to proper values before the solver is started. Weights are also applied in the scalar product, eq. (2.95), and in the vector norms, eq. (2.93) and (2.97), that are the volume of the cell times a number depending on which variable is represented. The weights for the turbulence variables was set to zero in this thesis since it gave the best performance.

2.6 Implicit Residual Smoothing

The CFL number can be increased and convergence to a steady state solution accelerated by smoothing the residuals implicitly. The time derivatives in each cell, i.e. the residuals, are smoothed at each stage in the Runge-Kutta cycle by an approximate factorization technique so that smoothing is applied on cell tubes in one direction at a time for each block of the mesh. The smoothing operator can then be seen as a diffusion problem in one dimension as

$$\frac{\partial u}{\partial t} = \epsilon \frac{\partial^2 u}{\partial x^2} \tag{2.108}$$

where ϵ is a constant and u is an arbitrary variable. Applying central difference and backward Euler gives

$$\frac{1}{\Delta t}\left(u_j^{p+1} - u_j^p\right) = \frac{\epsilon}{\Delta x^2}\left(u_{j-1}^{p+1} - 2u_j^{p+1} + u_{j+1}^{p+1}\right) \tag{2.109}$$

where p is the time step index and j is the cell index. By replacing $\frac{\epsilon \Delta t}{\Delta x^2}$ with λ and u with a residual $\dot{u}$, this equation can be written as

$$-\lambda\, \dot{u}_{j-1} \;+\; (1+2\lambda)\, \dot{u}_j \;-\; \lambda\, \dot{u}_{j+1} = \dot{u}_j^{old} \tag{2.110}$$

The value of λ now determines the amount of smoothing on the residual $\dot{u}$. A matrix operator for each cell tube can be written as

$$A = \begin{bmatrix} 1+\lambda & -\lambda & & & \mathbf{0} \\ -\lambda & 1+2\lambda & -\lambda & & \\ & -\lambda & 1+2\lambda & -\lambda & \\ & & & \ddots & \\ \mathbf{0} & & & & \end{bmatrix} \tag{2.111}$$

if a zero gradient (Neumann) boundary condition is applied at both ends. This equation is applied to the cell tubes in all three directions of each block for all derivatives of the conservative variables in the state vector. Smoothing is first applied in the I direction, the result from this operation is smoothed in the J direction and the result from both these operations is finally smoothed in the K direction. This approximate factorization procedure for the state vector derivative can be written as

- I direction smoothing. Loop over J and K and perform:

$$-\lambda\,\dot{Q}^{*}_{I-1,J,K} + (1+2\lambda)\,\dot{Q}^{*}_{I,J,K} - \lambda\,\dot{Q}^{*}_{I+1,J,K} = \dot{Q}^{org}_{I,J,K} \tag{2.112}$$

- J direction smoothing. Loop over I and K and perform:

$$-\lambda\,\dot{Q}^{**}_{I,J-1,K} + (1+2\lambda)\,\dot{Q}^{**}_{I,J,K} - \lambda\,\dot{Q}^{**}_{I,J+1,K} = \dot{Q}^{*}_{I,J,K} \tag{2.113}$$

- K direction smoothing. Loop over I and J and perform:

$$-\lambda\,\dot{Q}^{new}_{I,J,K-1} + (1+2\lambda)\,\dot{Q}^{new}_{I,J,K} - \lambda\,\dot{Q}^{new}_{I,J,K+1} = \dot{Q}^{**}_{I,J,K} \tag{2.114}$$

The new time derivative, $\dot{Q}^{new}$, is then used to update the solution. Using this approach, the CFL number can be increased by a factor of about $\sqrt{1+4\lambda}$ as shown by e.g. Turkel *et al.* (1991). They also present a method for how to modify λ in cells with high aspect ratios. However, a constant value of $\lambda \approx 1$ and $CFL \approx 2$ was used in this thesis. All time levels were smoothed separately in the time spectral computations. Smoothing in time was also tested, but this made even the most simple computations unstable if the Newton-GMRES algorithm was not used. These computations converged when Newton-GMRES was used but with a penalty on performance.

There were some problems with smoothing of the turbulence variables. Stable computations were obtained by using limiters both before and after the smoothing step, but some unphysical behavior could still be identified. The solution used in this thesis is to exclude the turbulence variables from the smoothing and use a separate, lower, CFL number for them. Another solution may be to use a partial implicit treatment of the turbulence model to make it more robust, such as for instance Zhao (1997) does.

2.7 Acoustic Analogies

Equations for sound propagation are used to evaluate the noise at a distance away from the source region. This can be used to save computational time since the mesh in the CFD computation does not have to be extended far out into the surroundings even if the noise is to be evaluated there. The noise sources are instead identified and an integral equation is solved to obtain the noise at an observer location. It is assumed that the wave equation is valid in the region from the source to the observer, and this is usually a good approximation.

There are mainly two approaches for obtaining the noise at observer locations in the far-field regions. The first, named after Kirchhoff (1883), is a surface integral method where the noise sources are contained by a closed surface as in figure 2.6. The pressure, and derivatives of it, at the surface, $\partial\Gamma$, is integrated and the noise can be obtained at an arbitrary location outside the surface. It is important that the surface lies outside of the hydrodynamic region of the flow because the wave equation must be valid for all the pressure disturbances that reach the surface.

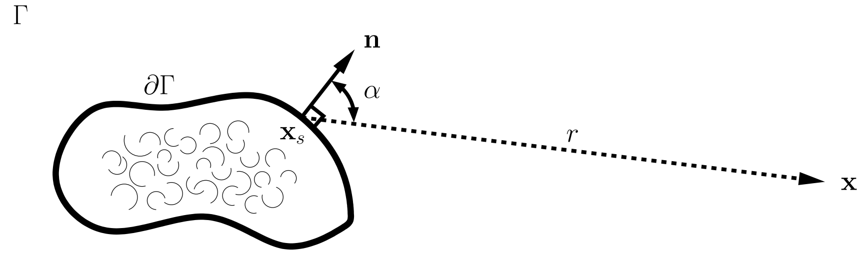

Figure 2.6: Kirchoff's surface integral method for calculation of noise at an observer, x

The other approach is to take the noise sources into account directly. It started with Lighthill (1952), who combined the nonlinear flow equations with linear theory of acoustics and identified the stress tensor, T_{ij}, named after him, as a source of noise:

$$T_{ij} = \rho u_i' u_j' + (p' - c_\infty^2 \rho')\delta_{ij} - \tau_{ij} \tag{2.115}$$

The Lighthill stress tensor can be seen as the turbulence source, and it acts as a quadrupole. Curle (1955) later extended the theory to account for solid surfaces in the turbulent flow, i.e. dipole sources, and Ffowcs Williams & Hawkings (1969) made the theory applicable also for moving solid surfaces and added the monopole source. Figure 2.7 shows the set-up for a FWH calculation.

The FWH method was used in Papers III and VI, and the original formulation includes both a volume integral and surface integrals and can be written as

$$\begin{aligned} p'(\mathbf{x},t) = \; & \frac{1}{4\pi}\frac{\partial^2}{\partial x_i \partial x_j} \iiint\limits_{\Gamma} \left[\frac{T_{ij}}{r|1-M_r|}\right]_{ret} dV \\ & -\frac{1}{4\pi}\frac{\partial}{\partial x_i} \oint\!\!\oint\limits_{\partial\Gamma} \left[\frac{p' n_i}{r|1-M_r|}\right]_{ret} dS \\ & +\frac{1}{4\pi}\frac{\partial}{\partial t} \oint\!\!\oint\limits_{\partial\Gamma} \left[\frac{\rho_\infty v_j n_j}{r|1-M_r|}\right]_{ret} dS \end{aligned} \tag{2.116}$$

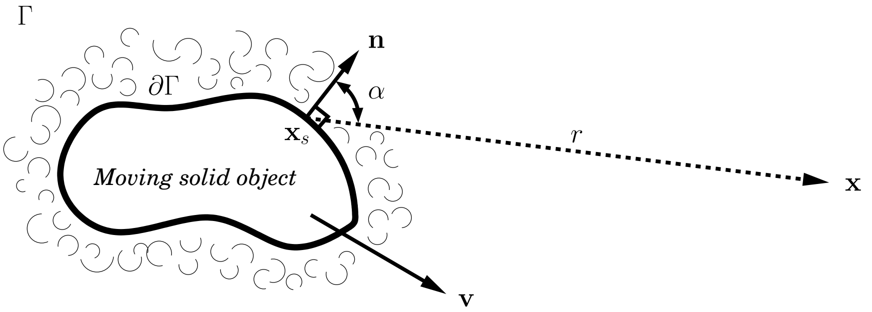

Figure 2.7: FWH method for calculation of noise at an observer, $\mathbf{x}$**.**

where $[\cdot]_{ret}$ means that the inside should be evaluated at a retarded time, $t - \frac{r}{c_\infty}$, i.e. the emission time. The three terms on the right hand side represent the quadrupole sources, dipole sources and monopole sources, respectively. The variable r is the distance from the integration point to the observer:

$$r = |\mathbf{x} - \mathbf{x}_s| \tag{2.117}$$

The Mach number relative to the observer is written as

$$M_r = \mathbf{M} \cdot \frac{(\mathbf{x} - \mathbf{x}_s)}{r} \tag{2.118}$$

where

$$\mathbf{M} = \frac{\mathbf{v}}{c_\infty} \tag{2.119}$$

Problems with accuracy may arise if eq. (2.116) is solved numerically. This is mainly because derivations in space must be done at the observer location. Brentner & Farassat (2003) made several reformulations of the FWH equation to make it more suitable for numerical implementation. Their "Formulation 1" was used in this thesis and is given by

$$p'(\mathbf{x}, t) = \frac{1}{4\pi c_\infty}\frac{\partial}{\partial t}\oiint_{\partial\Gamma}\left[\frac{p' cos(\alpha) + \rho_\infty c_\infty v_n}{r|1 - M_r|}\right]_{ret} dS + \frac{1}{4\pi}\oiint_{\partial\Gamma}\left[\frac{p' cos(\alpha)}{r^2|1 - M_r|}\right]_{ret} dS \tag{2.120}$$

The quadrupole term is neglected and there is only a time derivative in the equation, i.e. no derivations in space. The velocity of the surface in the normal direction is calculated as

$$v_n = \mathbf{v} \cdot \mathbf{n} \tag{2.121}$$

and

$$cos(\alpha) = \frac{(\mathbf{x} - \mathbf{x}_s) \cdot \mathbf{n}}{r} \tag{2.122}$$

is a measure of the surface element direction towards the observer.

Equation (2.120) is implemented as a source-time-dominant algorithm. This means that the time when the surface pressure was sampled is used as a reference time instead of the retarded time at the observer. The time when the emission from a surface element will reach the observer is calculated as $t + \frac{r}{c_\infty}$ and the contribution is then interpolated to two positions in the observer pressure signal. A validation test case for the FWH implementation is included in Appendix A.

The paper by Brentner & Farassat (2003) also has a permeable surface formulation of the FWH equation that can be used like the Kirchhoff method. The advantage of the permeable FWH formulation is that it is not as sensitive to hydrodynamic pressure fluctuations and the surface integral can thus be located closer to the sound source.

Chapter 3

Summary of Papers

THIS chapter gives a short summary of the work done and the results reported in the six papers on which this thesis is based.

3.1 Paper I

3.1.1 Motivation and Background

Paper I presents the results of a simulation of the rotor wake response on a stator vane in a fan stage. Two different techniques are used to predict the acoustic response: one time domain nonlinear URANS method with chorochronic periodic b.c. and one frequency domain LNSE method.

3.1.2 Work and Results

The fan stage has a rotor stator vane count ratio of about 1:1.56. A frequency domain LNSE solver that has been validated against independent data is used as a reference. There were some problems with what seemed to be reflections in the buffer layer in the nonlinear URANS simulations. Also, the nonlinear solution was obtained with a coarser mesh and the results were thus not as good as those of the reference computation.

3.1.3 Comments

The purpose of Paper I was to evaluate the time lagged periodic boundary condition (chorochronic periodicity). When a time shift is done in the periodic boundary condition using Fourier coefficients, something that stabilizes the computation in time is needed. The method chosen in Paper I was to make the periodic boundaries absorbing. This was shown later to be a bad choice, since it produces a non-negligible amount of extra spatial dissipation. It is also questioned whether this method had anything to do with the reflections seen in the simulation. Nonetheless, for simple test cases, the method in Paper I seemed to work well, while it produces poor results for more realistic cases.

3.2 Paper II

3.2.1 Motivation and Background

Paper II gives a presentation of the same simulation as in Paper I with some changes in the time lagged periodic boundary condition.

3.2.2 Work and Results

The same fan stage as in Paper I and the same reference solution are used, but here both the nonlinear solution and the reference linear solution were obtained with the same mesh. The chorochronic periodic boundary condition was stabilized with a temporal damping term, instead of as in Paper I, with a method that produces extra spatial dissipation.

3.2.3 Comments

The results reported in Paper II are much better than those in Paper I, but there are still differences in sound generation compared to the linear solver. These can be referred to differences in the wake development and the physics captured between LNSE and URANS. The mean flow and the turbulence quantities are frozen in the LNSE simulation, but everything is solved together in the URANS computation, allowing the wake to interact with both the mean flow and the turbulence quantities. The wake changes somewhat during the short path from the inlet to the stator vane. This has an impact on the amplitude of the pressure modes downstream of the stator.

The URANS simulation was done with both three and six harmonics in the chorochronic periodic boundary condition and also with domains that included both one and two stator vanes. There were no significant differences between these simulations.

3.3 Paper III

3.3.1 Motivation and Background

Paper III gives a presentation of the results of a simulation of a turbulent rotor wake response on a stator vane in a fan stage. A hybrid RANS/LES method was used and the inlet wake was triggered into turbulent mode by adding synthetic fluctuations. Both the tone noise and the low to medium frequency broadband noise can be captured with this method by using at least three stator vane passages and chorochronic periodic boundary conditions with buffer zones. This method saves computational time compared to a full 360° computation, which may be the only alternative.

3.3.2 Work and Results

Two different cases were compared where the reference case fan stage has a rotor stator vane count ratio of 2:3 and the other is a low tone noise case with a rotor stator vane count ratio of about 1:1.56. The reference case was simulated with standard periodic boundary conditions while the low tone noise case was computed with chorochronic boundary conditions and buffer zones. The results show that the synthetic turbulent fluctuations added at the inlet quickly adapt to the mean wake and make it turbulent. As expected, the tone noise changes with the change in blade count ratio. The low frequency broadband noise is also different between the two cases, but the medium to high frequency is not.

3.3.3 Comments

The purpose of the work reported in Paper III was to evaluate the time lagged periodic boundary condition (chorochronic periodicity) together with chorochronic buffer zones mainly for broadband noise simulations. The number of samples was somewhat low in the results but the computations were continued after the paper was published so that a total of 990 samples was obtained for each case (compared to 660 in Paper III). A third case was also computed where the rotor stator vane count ratio is 2:3 but the chorochronic b.c. with buffer zones was used. There is then no time lag in the periodic boundary, but the b.c. together with the buffer zones filter the flow from stochastic perturbations in the area close to the periodic boundaries. The results shown in figure 3.1 are treated in the same way as in Paper III, i.e. a FWH integration is performed for the tone and broadband source separately, and the broadband part is filtered in third octave bands. It can be seen that the chorochronic buffer zone has an effect on the low frequency broadband noise when comparing the two cases with a rotor stator blade count ratio of 2:3. The two cases with chorochronic buffer zones (CB) allow for a more direct comparison of a small change in the blade count ratio, and it can be seen that this has almost no effect on the broadband noise.

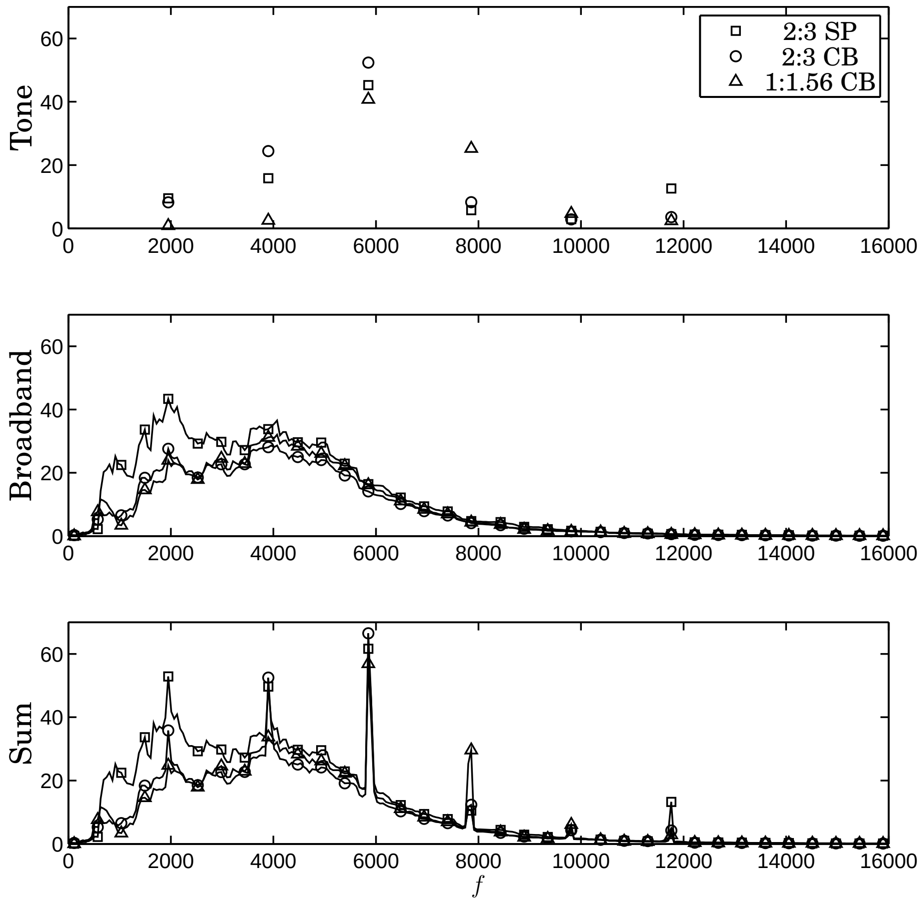

Figure 3.1: Power spectrum of FWH evaluation for tone and broadband noise. The case with a rotor stator vane count ratio of 2:3 is calculated both with standard periodic b.c. (SP) and with chorochronic periodic b.c. and chorochronic buffer zones (CB).

3.4 Paper IV

3.4.1 Motivation and Background

Paper IV presents a method for using buffer layers at the inlet of a rotor wake/stator computation to reduce spurious reflections of acoustic waves at the inlet boundary. The unsteady rotor wake is specified at the inlet to the stator domain, and this prohibits the use of a standard buffer layer technique since it would dissipate the wake that is supposed to impinge on the stators. On the other hand, the deterministic part of the rotor wake is stationary in the rotor frame of reference, and by having an inlet zone that rotates with the rotor wake, a standard buffer layer technique can be used in the rotating inlet zone without destroying the wake. A 1D absorbing boundary condition was used as a reference, but a more advanced 2D absorbing b.c. was also tested and compared to the inlet buffer layer technique.

3.4.2 Work and Results

The same 3D test case used in Papers I-III was used in Paper IV as a reference; named case I. A part of the inlet was modified to fit the rotor pitch, case II, and this zone was solved in a rotating frame of reference both with and without a buffer layer. The different boundary conditions were then evaluated with a 3D mode analysis tool that can measure to what extent an approaching wave is reflected. Table 3.1 lists the cases that were computed in Paper IV.

Table 3.1: Specification of cases in Paper IV. Case I and case II is solved without a rotating inlet zone and with a rotating inlet zone, respectively.

Case I a	1D absorbing inlet
Case I b	2D absorbing inlet
Case II a	1D absorbing inlet **with** inlet buffer layer
Case II b	1D absorbing inlet **without** inlet buffer layer

There were problems with the 2D absorbing boundary condition. The reason was found to be a mode that, according to 2D analysis, went from being cut-on to being cut-off inside the duct. This made the 2D absorbing b.c. somewhat unstable. The entire flow field was disturbed by this, and the results with the 2D b.c. were therefore not good.

3.4.3 Comments

A somewhat surprising result was that the 1D absorbing boundary condition performed much better in the rotating frame of reference than in the stator frame of reference. A case with a rotating inlet zone without a buffer layer was simulated and compared to the reference case without a rotating inlet zone. The same 1D absorbing boundary condition was used in both these cases, but the 1D absorbing b.c. in the rotating frame of reference absorbed a larger portion of the approaching waves in five out of six cut-on modes analyzed. The reason for this can be argued to be that the rotor wake is stationary at the inlet boundary in the rotating frame of reference and the only unsteadiness is the acoustic modes. This seems to have a beneficial effect on the 1D analysis at the boundary.

A solution to the instability in the 2D absorbing boundary condition is to exclude modes that are cut-off or close to cut-off in the boundary condition. Results of this kind of simulation are presented in Paper V.

3.5 Paper V

3.5.1 Motivation and Background

This paper is a continuation of Paper IV and investigates whether a varying value of the damping factor in the buffer layer can improve absorption. The 2D absorbing boundary condition is modified to exclude cut-off and close to cut-off modes. The harmonic balance technique is also tested as a tool for tone noise predictions.

3.5.2 Work and Results

Case I a in Papers IV and V is exactly the same, i.e. has the same results. Case I b in Paper IV is the same as Case I b in Paper V except for the modification in the 2D absorbing boundary condition. The results with the 2D absorbing b.c. were greatly improved in Paper V as compared to those in Paper IV. Case II b in Paper IV is exactly the same as Case II a in Paper V, i.e. the results are the same. Case II b and c in Paper V are exactly the same cases, but Case II b is solved with a standard time stepping procedure and Case II c is solved with the harmonic balance technique. These two cases also have varying values of the damping factor in the buffer layer, which improved the absorption for all modes except the one with the largest wave length compared to case II a. The results in Case II b and c, i.e. standard time stepping and the harmonic balance technique, were generally very similar. Table 3.2 lists the cases that were computed in Paper V.

Table 3.2: Specification of cases in Paper V. Case I and case II is solved without a rotating inlet zone and with a rotating inlet zone, respectively.

Case I a	1D absorbing inlet.
Case I b	2D absorbing inlet.
Case II a	1D absorbing inlet **without** inlet buffer layer.
Case II b	1D absorbing inlet **with** inlet buffer layer.
Case II c	1D absorbing inlet **with** inlet buffer layer solved with the harmonic balance technique.

3.5.3 Comments

The total length of the inlet buffer layer was a little too short for some of the cut-on pressure modes, and the length was not increased when a varying value of the damping factor was introduced in Paper V. This may explain why there were more reflections in two of the cut-on modes when a varying value of the damping factor was used, i.e. comparing the results of case II a in Paper IV and the results of case II b in Paper V. The other four cut-on modes were better absorbed with a varying value of the damping factor compared to a constant.

A case without a rotating inlet zone was simulated with the harmonic balance technique. However, this case did not converge because of a slowly growing pressure mode close to the inlet hub. The Newton-GMRES method was used in this case after Paper V was published; the method suppressed the instability in the solver, and converged results were obtained for this case as well. These results were generally in a good agreement with the results from using standard time stepping.

Case II c has also been solved using the Newton-GMRES method after Paper V was published. The residuals reached to a lower level when this method was used. Figure 3.2 shows pressure modes between the inlet and the stator of case II c together with results using the Newton-GMRES method. Results with three, four and five harmonics within the time spectral treatment are also shown in figure 3.2. It can be seen that there is a small difference between case II c and the corresponding case solved with the Newton-GMRES method, mainly in the first BPF. Truncation errors can be seen in the third BPF in the case solved with three harmonics in the time spectral treatment but the cases with four, five and six harmonics, solved with the Newton-GMRES method,

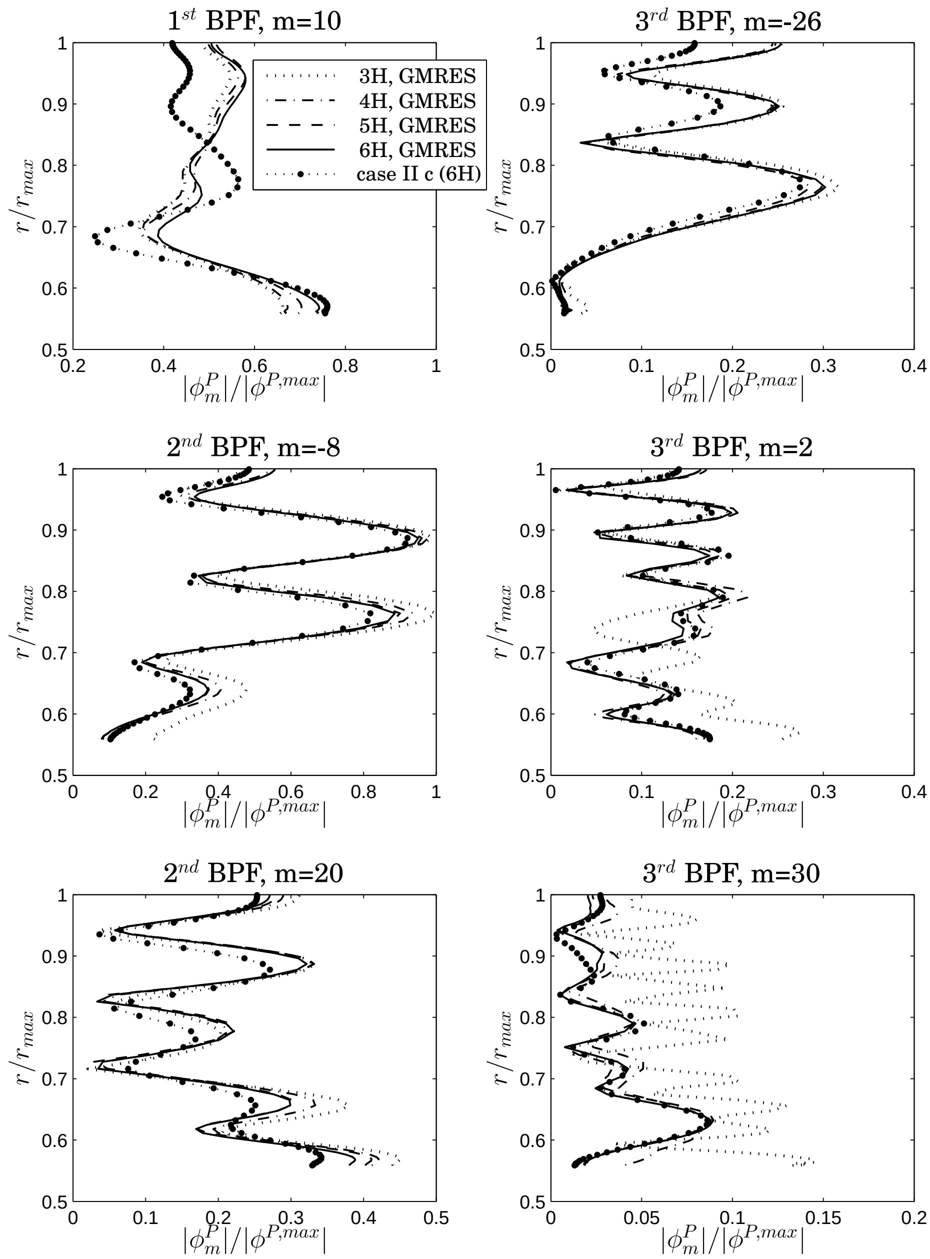

Figure 3.2: Cut-on pressure modes between inlet and stator. All cases are solved with the harmonic balance technique. Four of the cases use the Newton-GMRES method and are solved with three, four, five and six harmonics respectively within the time spectral treatment. The results of case II c presented here are the same as the results of case II c in Paper V, i.e. solved without the Newton-GMRES method.

are in good agreement. It should be noted that only three harmonics of the rotor wake are specified at the inlet and anything that appear in harmonic four, five and six are due to nonlinear effects.

3.6 Paper VI

3.6.1 Motivation and Background

The purpose of Paper VI was to develop a performance model / preliminary design tool for counter-rotating propfans and to then compare it with a more detailed CFD analysis. The CFD computation was also used to predict the noise from the propellers via a FWH surface integral method. The aim was to validate these models against open literature data on the counter-rotating propellers developed in the 1980s.

3.6.2 Work and Results

The GE36 F7-A7 propellers were designed/created according to open literature data, and the performance model matched the design targets and the test results very well. On the other hand, the CFD results predicted a much higher thrust and a lower efficiency than both the preliminary design tool predictions and the test results. The reason for this difference is that the pitch angle settings in the tests were modified from the settings specified in the design report (GE36 Design and System Engineering, 1987) to fit the design goals. A few iterations were done with the pitch angle settings in the preliminary design tool to fit the CFD results, and it seems that, while the trends are predicted correctly, the exact pitch angle setting is not.

The only noise measurements found in the literature for the chosen operating point were measurements of the first BPF. The agreement was generally very good, but the first BPF unfortunately does not include any interaction noise in this case. A steady and an unsteady CFD simulations were both made, and the interaction noise was then identified as the difference in noise between the two simulations. The obtained amount of interaction noise looks reasonable but was not verified against measurements.

3.6.3 Comments

The exact pitch angle settings used in the experiments were not found in the open literature and thus a truer comparison of CFD and experiments could not be made. The initial aim was to make a few design iterations, e.g. other pitch angle settings, and to compute other operating points with CFD as well. This was not done however owing to time limitations.

Many shocks were present in the solution, and the applicability of the FWH method used can be questioned. A better approach may be to use a permeable FWH formulation and a closed surface outside the blades. It can be argued that there will be less interaction noise if the nonlinear effects are treated in a more correct way. A validation case is included in Appendix A and the results points towards an overprediction of sound from the FWH surface pressure integration method when the flow becomes nonlinear.

Chapter 4

Concluding Remarks

THE TONAL ACOUSTIC RESPONSE from rotor wake interactions with stators using chorochronic periodicity and unsteady CFD was validated against a linearized Navier-Stokes equations solver method.

The chorochronic periodic boundary condition was also used in combination with a chorochronic buffer zone for predictions of broadband noise for the rotor wake interaction with stators. A method based on Hybrid RANS/LES was then used to obtain the "medium" frequency broadband noise, i.e. from about 1000 to 6000 Hz.

A chorochronic interface was also developed and validated against a sliding grid interface. The chorochronic interface was used to make it possible to use an inlet buffer layer for rotor wake/stator computations.

A 2D absorbing boundary condition was implemented and tested in a 3D computation. The performance was evaluated using a 3D modal decomposition tool.

The harmonic balance technique was also tested for tone noise predictions. This is a time spectral method that was verified against the standard time stepping technique, and it was also combined with chorochronic boundary conditions and interface.

4.1 Work done and experiences

A summary of the work done and experiences of the methods used in this thesis is given in the following paragraphs.

4.1.1 Chorochronic Periodicity

The implementation of a Fourier-based time-lagged periodic boundary condition is done by continuously updating finite Fourier series in the area close to the boundary and then evaluating the series on the other side at a different time corresponding to the pitch-to-pitch time lag.

Stability can be obtained by introducing extra numerical damping in the area close to the periodic boundary.

Temporal damping, which uses the Fourier coefficients to damp out non-periodic flow phenomena, can be used to stabilize computations without introducing extra spatial dissipation.

The model has been validated by comparing results obtained from simulations with standard periodic boundary conditions and results from a LNSE method previously validated against independent data.

4.1.2 Chorochronic Buffer Zone

The temporal damping used to make the chorochronic periodic boundary condition stable can also be used in Hybrid RANS/ LES computations to damp stochastic perturbations close to the periodic boundaries.

At least three stator vane passages are discretized, and chorochronic buffer zones are used in the area close to the pitchwise boundaries together with chorochronic periodic boundary conditions.

The rotor wake is specified at the inlet and synthetic turbulent fluctuations are added to trigger the flow into turbulent mode.

The center vane is relatively unaffected by the filtering at the pitchwise boundaries, and the pressure fluctuations on it can be used as a source for both tone and broadband noise.

4.1.3 Chorochronic Rotor-Stator Interface

A general Fourier-based interface was implemented. It is not restricted to computations with the same domain size in the tangential direction, as is needed when a standard sliding grid interface is used.

Time Fourier series of the flow close to the interface are calculated using a moving average technique.

Time and space Fourier series of the modal content of the flow close to the interface are calculated by integrating the time Fourier series in space.

The modal content of the flow, i.e. the time and space Fourier coefficients, on one side of the interface is passed on to the other frame of reference and evaluated with a shift in frequency.

Validation of the interface was done by comparisons with simulations obtained with a standard sliding grid interface.

4.1.4 2D Absorbing Boundary Conditions

The modal content of the flow close to the boundary is obtained in the same way as in the chorochronic rotor-stator interface.

The axial and circumferential characteristics are calculated and extrapolated to ghost cells by using the associated wave numbers.

The 2D analysis is restricted to modes that are not too close to the transition from cut-on to cut-off or vice versa.

Stability can be obtained by excluding modes that are cut-off or close to cut-off from being extrapolated.

4.1.5 Buffer Layer

Unsteady flow is damped by the buffer layer through an additional source term in the governing equations.

A low-pass filter is used to update a reference state that is used in the damping term.

A function based on arcus tangent was used to alter the amount of damping in order to avoid high gradients in the beginning and at the end of the buffer layer.

A buffer layer at the inlet of a rotor wake/stator computation can be used if a part of the inlet rotates with the wake.

4.1.6 Hybrid RANS/LES

Turbulent fluctuations that are resolved by the mesh can be computed by using a hybrid RANS/LES method where only the unresolved turbulence is modeled.

The k-epsilon model is used in this thesis and the length scale is limited to about 20% of a typical cell size. The turbulence model then works as a Smagorinsky subgrid scale LES model everywhere except close to solid walls where the increased resolution results in a local URANS model.

4.1.7 Harmonic Balance Technique

Nonlinear periodic flows can be solved with the harmonic balance technique, which makes it suitable for rotor-stator interaction computations.

The state vector contains the solution at a discrete number of time levels that represent the periodic content in the flow.

A time spectral derivative is calculated from the solutions at different time levels and added as a source term to the governing equations.

A pseudo time technique is used to update the solution and iterate towards convergence.

A few extra frequencies may be added in the spectral treatment to avoid truncation errors in the frequencies that are of main interest.

Fourier based boundary conditions are easy to implement since there is no need for sampling to update the coefficients. The coefficients are calculated directly from the different time levels in the state vector.

4.1.8 Newton-GMRES

Convergence can be improved by using the Newton-GMRES method to iterate towards steady state.

Krylov vectors are obtained using an Arnoldi process. The derivative times a Krylov vector is approximated by using the time stepping routine in the CFD code.

The rate of convergence was greatly improved for the harmonic balance computations done in this thesis.

A slow instability was identified in one of the harmonic balance test cases. It was later suppressed by the Newton-GMRES method.

4.1.9 Implicit Residual Smoothing

The rate of convergence towards steady state can be improved by smoothing the residuals implicitly and increasing the CFL number.

Implicit residual smoothing was used with the harmonic balance technique; each time level should then be smoothed separately.

Smoothing of the turbulence variables was shown to be a bit problematic. The solution was to exclude them from the smoothing operation and use a separate CFL number.

4.1.10 FWH Sound Propagation

Acoustic analogies can be used when the sound is to be evaluated at a distance from the source. It is usually much cheaper to use an analogy instead of extending the mesh into the farfield.

A FWH method that includes monopole and dipole sources was used in this thesis. The surface pressure of vanes, blades, hub and shroud are used as sources.

The implementation was made with a formulation of the FWH equation that does not have derivations in space for better accuracy and performance.

The permeable FWH formulation, which uses a permeable surface that can be placed around the sources, is probably a better choice when strong shocks are present in the solution.

4.2 Final recommendations

After a lot of theoretical and technical discussions we have reached the end of the main part of this thesis. I would like to share my personal view on how things should be done to those who plan to work on this subject in the future. My recommendation for nonlinear tone noise predictions is to use the harmonic balance technique before using standard time stepping. The harmonic balance technique is a much more efficient tool when acceleration techniques such as the Newton-GMRES method and implicit residual smoothing are used, and no extra numerical damping is needed in the periodic boundary with time lag. The extra numerical damping, in the periodic boundary with time lag, may need to be tuned for each new case when standard time stepping is used. However, the harmonic balance technique is not an option for broadband noise predictions. The amount of frequencies that needs to be included in the spectral treatment would be too many to be efficiently handled, using this method at its current state. The hybrid RANS/LES method, using standard time stepping, is a promising candidate for broadband noise predictions and full 360^o computations can be avoided by using chorochronic buffer zones.

Deciding boundary conditions is another interesting issue, especially if the rotor is omitted in the calculation and the rotor wake specified at the inlet to the stator domain. A rotating inlet zone, where the rotor wake is stationary, can be added in tone noise predictions and it can improve the performance of simple boundary conditions. A standard buffer layer technique can also be added in the rotating inlet zone that can improve the total absorption of waves even more. I recommend this approach before using more complex types of boundary conditions, i.e. 2D or 3D absorbing b.c., for nonlinear cases. However, the rotating inlet zone at its current state can not be used in broadband noise predictions using hybrid RANS/LES. Stochastic perturbations should exist in the flow that may not fit the Tyler & Sofrin interaction modes and these can thus not be transferred by the Fourier based rotor-stator interface. Maybe the rotor must be included somehow in broadband noise predictions to be able to absorb waves that propagate upstream correctly; a buffer layer can be used upstream of the rotor.

The acoustic analogies provide some very powerful tools in certain situations. I have only used the "solid surface" FWH formulation and I think it performs surprisingly well in the validation test case, even when the flow becomes a bit nonlinear; see Appendix A. A similar study with the permeable FWH formulation would be interesting to see.

Bibliography

ANDERSSON, N. 2005 A study of subsonic turbulent jets and their radiated sound using Large-Eddy Simulation. PhD thesis, Division of Fluid Dynamics, Chalmers University of Technology, Gothenburg.

BARALON, S., ERIKSSON, L.-E., BILLSON, M. & ANDERSSON, N. 2005 Evaluation of advanced prediction methods for aero engine exhaust noise. No. 1190. The 17th ISABE meeting, Munich, Germany.

BODONY, D. J. 2006 Analysis of sponge zones for computational fluid mechanics. *J. Comp. Physics* **212** (2), 681–702.

BRENTNER, K. S. & FARASSAT, F. 2003 Modeling aerodynamically generated sound of helicopter rotors. *Progress in Aerospace Sciences* **39** (2-3), 83–120.

BROWN, P. N. & SAAD, Y. 1994 Convergence theory of nonlinear newton-krylov algorithms. *SIAM J. Optimization* **4** (2), 297–330.

CHASSAING, J. C. & GEROLYMOS, G. A. 2007 Time-domain implementation of nonreflecting boundary-conditions for the nonlinear Euler equations. *Applied Mathematical Modelling* **31**, 2172–2188.

COLONIUS, T. 2004 Modeling artificial boundary conditions for compressible flow. *Annu. Rev. Fluid Mech.* **36**, 315–345.

COLONIUS, T., LELE, S. K. & MOIN, P. 1993 Boundary conditions for direct computation of aerodynamic sound generation. *AIAA Journal* **31** (9), 1574–1582.

CURLE, N. 1955 The influence of solid boundaries on aerodynamic sound. *Proc. Roy. Soc.* **A 231**, 505–514.

ENGQUIST, B. & MAJDA, A. 1977 Absorbing boundary conditions for numerical simulation of waves. *Math. Comp.* **31** (139), 629–651.

ERDOS, J. I., ALZNER, E. & MCNALLY, W. 1977 Numerical solution of periodic transonic flow through a fan stage. *AIAA Journal* **15** (11), 1559–1568.

ERIKSSON, L.-E. 1995 Development and validation of highly modular flow solver versions in g2dflow and g3dflow. Internal report 9970-1162. Volvo Aero Corporation, Sweden.

FFOWCS WILLIAMS, J. E. & HAWKINGS, D. L. 1969 Sound generated by turbulence and surfaces in arbitrary motion. *Phil. Trans. Roy. Soc.* **A 264**, 321–342.

FREUND, J. B. 2001 Noise sources in a low-Reynolds-number turbulent jet at Mach 0.9. *Journal of Fluid Mechanics* **438**, 277–305.

GE36 DESIGN AND SYSTEM ENGINEERING 1987 Full scale technology demonstration of a modern counterrotating unducted fan engine concept - design report. NASA-CR-180867.

GEROLYMOS, G. A., MICHON, G. J. & NEUBAUER, J. 2002 Analysis and application of chorochronic periodicity in turbomachinery rotor/stator interaction computations. *J. Propulsion and Power* **18**, 1139–1152.

GILES, M. B. 1988*a* Calculation of unsteady wake/rotor interaction. *Journal of Propulsion* **4** (4), 356–362.

GILES, M. B. 1988*b* Non-reflecting boundary conditions for the Euler equations. Tech. rep. tr 88-1. Cambridge, MA: MIT.

GILES, M. B. 1990 Non-reflecting boundary conditions for euler equation calculations. *AIAA Journal* **28** (12), 2050–2058.

GOPINATH, A. K., VAN DER WEIDE, E., ALONSO, J. J., JAMESON, A., EKICI, K. & HALL, K. C. 2007 Three-dimensional unsteady multistage turbomachinery simulations using the harmonic balance technique. No. 892. The 45th AIAA Aerospace Sciences Meeting and Exhibit, Reno, Nevada.

HALL, K. C., THOMAS, J. P. & CLARK, W. S. 2002 Computation of unsteady nonlinear flows in cascades using a harmonic balance technique. *AIAA Journal* **40**, 879–886.

HEDSTROM, G. W. 1979 Nonreflecting boundary condition for nonlinear hyperbolic systems. *J. Comp. Phys.* **30**, 222–237.

HUBBARD, H. H. 1994 *Aeroacoustics of Flight Vehicles*. Acoustical Society of America, ISBN 1-56396-407-4.

KIRCHHOFF, G. R. 1883 Zur theorie der lichtstrahlen. *Annalen der Physik und Chemie* **18**, 663–695.

KOYA, M. & KOTAKE, S. 1985 Numerical analysis of fully three-dimensional periodic flows through a turbine stage. *Journal of Engineering for Gas Turbines and Power* **107**, 945–952.

LEBRUN, M. & FAVRE, C. 2004 Fan-ogv unsteady Navier-Stokes computation using an adapted acoustic mesh. The 10th AIAA/CEAS Aeroacoustics Conference, Manchester, United Kingdom.

LI, H. D. & HE, L. 2001 Single-passage solution of three-dimensional unsteady flows in a transonic fan rotor. *Proceedings of the Institution of Mechanical Engineers, Part A: Journal of Power and Energy* **215**, 653–662.

LI, H. D. & HE, L. 2002 Single-passage analysis of unsteady flows around vibrating blades of a transonic fan under inlet distortion. *ASME Journal of Turbomachinery* **124**, 285–292.

LIGHTHILL, M. J. 1952 On sound generated aerodynamically, I. General theory. *Proc. Roy. Soc.* **A 211**, 564–587.

RICHARDS, S. K., ZHANG, X., CHEN, X. X. & NELSON, P. A. 2004 The evaluation of non-reflecting boundary conditions for duct acoustic computation. *J. Sound Vib.* **270**, 539–557.

SAAD, Y. & SCHULTZ, M. H. 1986 GMRES: A generalized minimal residual algorithm for solving nonsymmetric linear systems. *SIAM J. Sci. and Stat. Comput.* **7** (3), 856–869.

SCHNELL, R. 2004 Numerische simulation des akustischen nahfeldes einer triebwerksgebläsestufe. PhD thesis, Fakultät V – Verkehrs– und Maschinensysteme der Technischen Universität Berlin.

STRIDH, M. 2006 Modeling unsteady flow effects in 3d throughflow calculations. PhD thesis, Department of Applied Mechanics, Division of Fluid Dynamics, Chalmers University of Technology, Gothenburg.

STRIDH, M. & ERIKSSON, L.-E. 2005 Modeling unsteady flow effects in a 3d transonic compressor. ASME Turbo Expo, Reno-Tahoe, Nevada, USA.

TURKEL, E., SWANSONN, R. C., VATSA, V. N. & WHITE, J. A. 1991 Multigrid for hypersonic viscous two- and three-dimensional flows. NASA/CR-187603.

TYLER, J. M. & SOFRIN, T. G. 1962 Axial flow compressor noise studies. *SAE Transactions* **70**, 309–332.

VERDON, J. M. 2001 Linearized unsteady aerodynamic analysis of the acoustic response to wake/blade-row interaction. NASA/CR-2001-210713.

YAN, J., MOCKETT, C. & THIELE, F. 2005 Investigation of alternative length scale substitutions in detached-eddy simulation. *Flow, Turbulence and Combustion* (74), 85–102.

ZHAO, Y. 1997 Stable computation of turbulent flows with a low-reynolds-number k-epsilon turbulence model and explicit solver. *Advances in Engineering Software* **28** (8), 487–499.

Appendix A

Oscillating Sphere Validation Test Case

THE IMPLEMENTATION of "formulation 1" of the FWH method given by Brentner & Farassat (2003) is validated by computing the sound generated by an oscillating sphere. A 2D axisymmetric Euler solver is modified so that it can be used in an oscillating frame of reference. The surface of the sphere is created by a half circle around the origin with 101 mesh points and a radius of 1 meter. The outer bound is also a half circle at a radius of 30 meters, and the axis line is meshed with 1451 equidistant mesh points. The sphere oscillates along the axis, and a zoom-in on the sphere in the 2D mesh is shown in figure A.1.

The solver is used in a time accurate mode, and the number of time steps is set to a high enough value so that a periodic solution is obtained. Seven different cases are calculated in this manner, and the specifications for each case are shown in table A.1. The frequency and ambient conditions are kept constant, and the amplitude of the oscillation is varied. The maximum velocity of the sphere will vary with the amplitude; it is also tabulated. All cases were simulated for 15 periods before the sampling started, and all cases except case 7 converged to a periodic solution in that time. Case 7 is quite extreme, and separation occurred at the surface of the sphere, which made this case harder to converge. The somewhat non-periodic solution is nevertheless used in the comparison with FWH.

Instantaneous contours of static pressure for case 4 are shown in figure A.2 along with the observer locations, where the CFD solution is compared to the FWH integration. Point "c" is chosen so that the relative velocity between the sphere and this location is subsonic even for case 7.

The surface pressure in the 2D solution is sampled 50 times over one period and then interpolated to a 3D surface mesh shown in figure

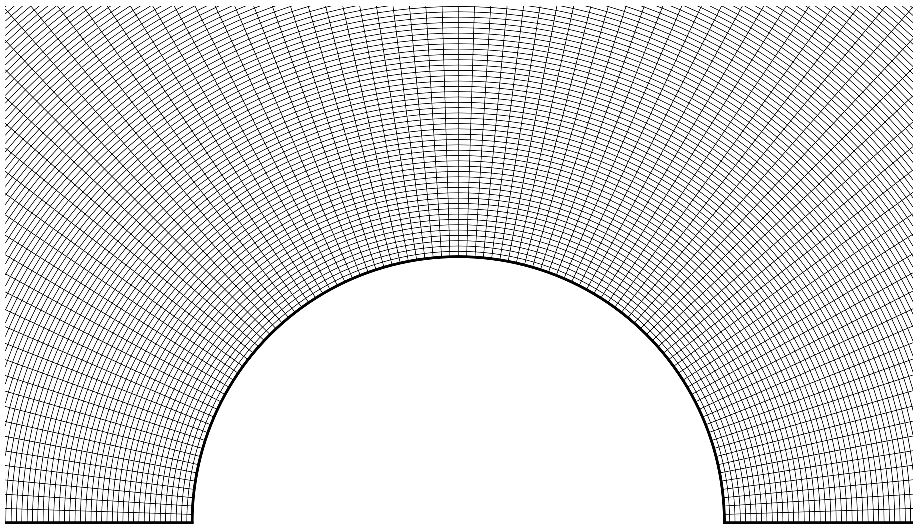

Figure A.1: 2D axi-symmetric mesh of a sphere. The radius of the sphere is one meter.

A.3. The 3D surface mesh and surface pressure from the 2D axisymmetric solution are then used in the FWH code to obtain the pressure fluctuations at the observer locations in figure A.2. The FWH integration must be done over a few periods since erroneous data are produced in the beginning and at the end of the observer pressure signal due to incomplete data at both ends. This happens since different surface elements contribute to different observer time steps in the source-time-dominant implementation.

The fluctuating static pressure for all cases at points “a”, “b” and “c” is shown in figure A.4, A.5 and A.6 respectively. It can be seen that the agreement is almost exact for cases 1 and 2 and there are only small variations in amplitude for cases 3 and 4. The differences are larger for case 5 mainly due to a shock that is present in the CFD results but not in the FWH evaluation. The FWH prediction is quite good at point “a” for cases 6 and 7 but the CFD results are overpredicted at points “b” and “c”. Some discrepancies are expected since there are nonlinear effects that are captured by the CFD computation but not by the FWH prediction, i.e. nonlinear propagation of pressure waves and unsteady shock wave interaction. Figure A.7 shows instantaneous pressure contours for case 6, and it can be seen that shocks are present in the entire domain. A more suitable way to predict the noise for cases

Table A.1: Specification of cases for the oscillating sphere validation test case

Case	f $[Hz]$	a $[m]$	$\lvert\mathbf{v}\rvert_{max}$ $[m/s]$	c_∞ $[m/s]$	ρ_∞ $[kg/m^3]$
1	54.59	0.002915	1.0	343.0	1.21
2	54.59	0.02915	10.0	343.0	1.21
3	54.59	0.1458	50.0	343.0	1.21
4	54.59	0.2915	100.0	343.0	1.21
5	54.59	0.5831	200.0	343.0	1.21
6	54.59	1.0	343.0	343.0	1.21
7	54.59	1.458	500.0	343.0	1.21

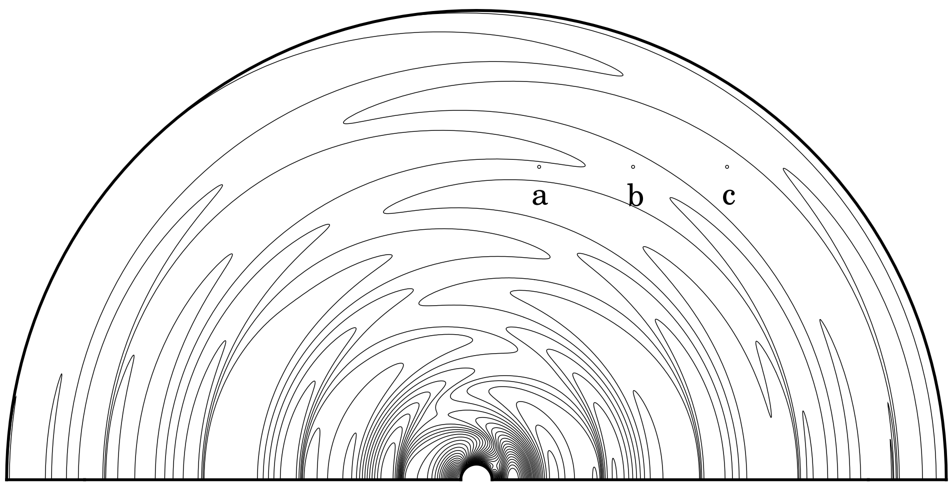

Figure A.2: Instantaneous contours of static pressure for case 4. The sphere is oscillating around $(0, 0)$ and the observer positions a, b and c are located at $(4, 20)$, $(10, 20)$ and $(16, 20)$ respectively.

6 and 7 would be to use another formulation of the FWH equation that can handle nonlinear effects in a better way or to use the permeable surface formulation and place the integration surface outside of the heavy nonlinear region close to the sphere.

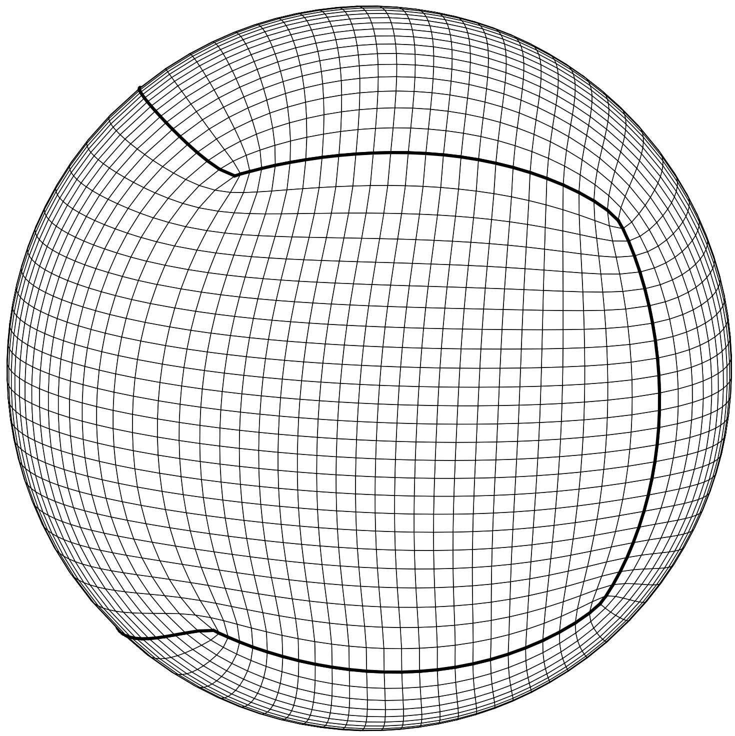

Figure A.3: 3D surface mesh of a sphere. The radius of the sphere is one meter.

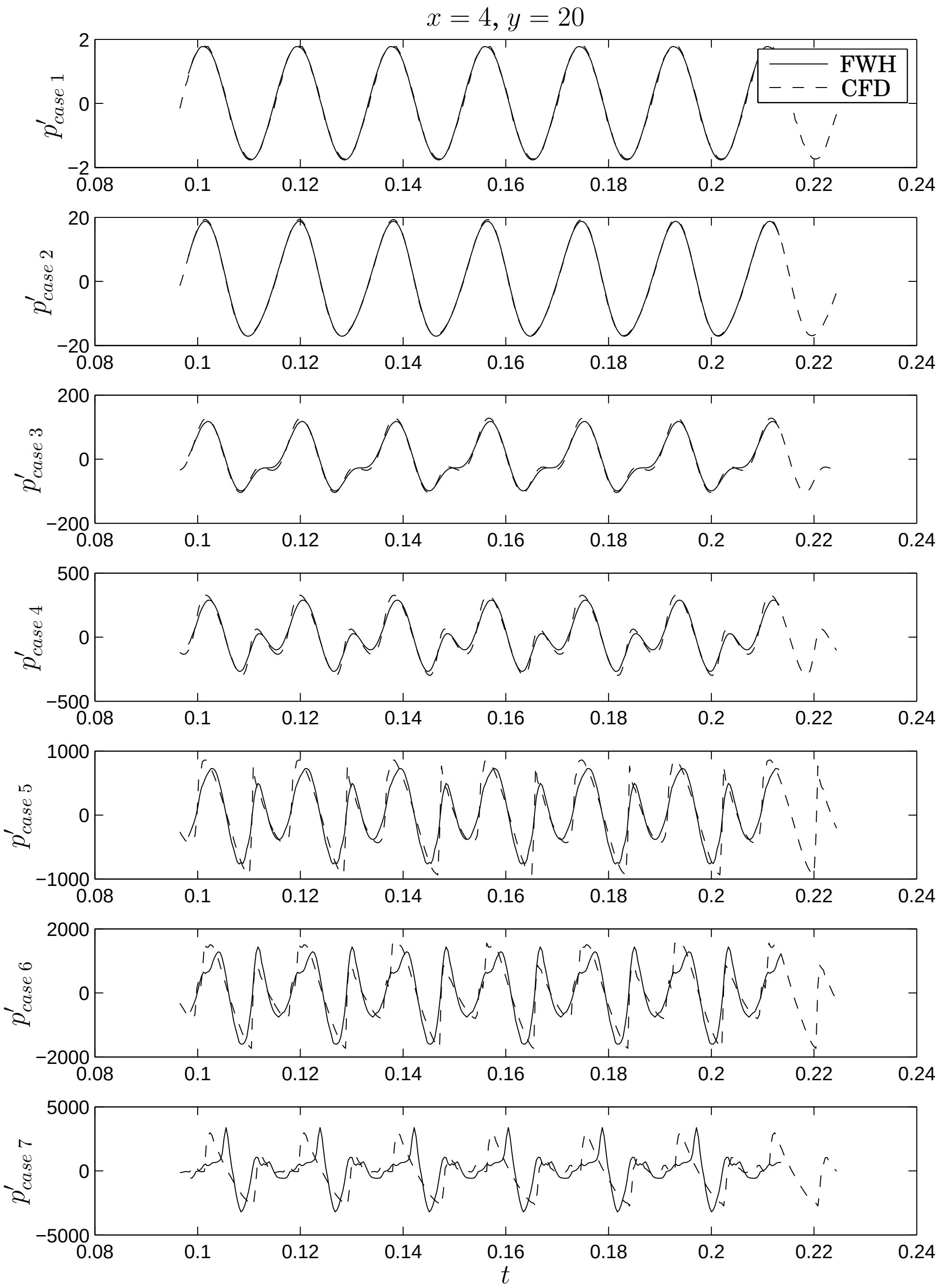

Figure A.4: Pressure fluctuations for cases 1-7 at point "a" in figure A.2 for both the FWH prediction and CFD data

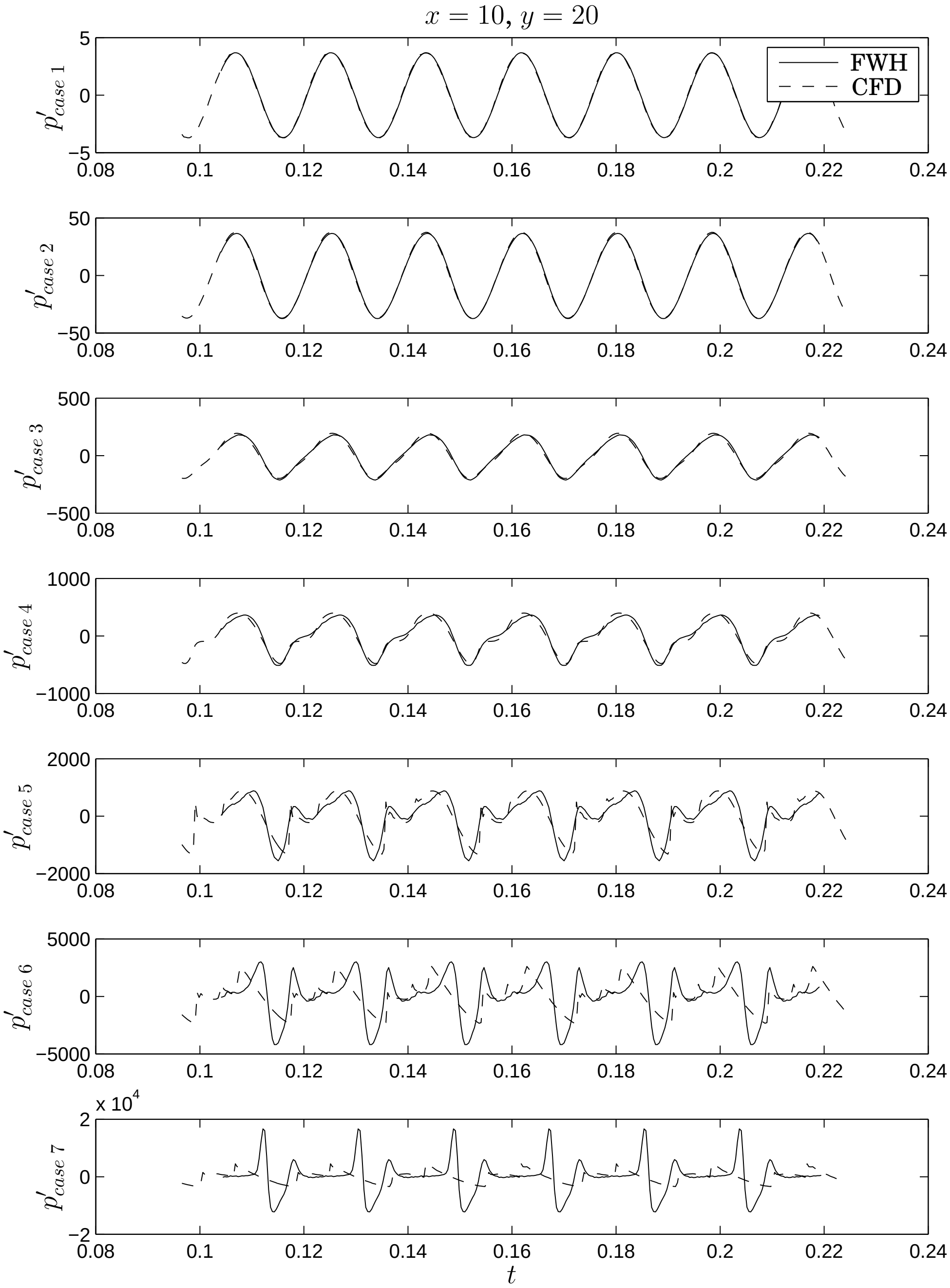

Figure A.5: Pressure fluctuations for cases 1-7 at point "b" in figure A.2 for both the FWH prediction and CFD data

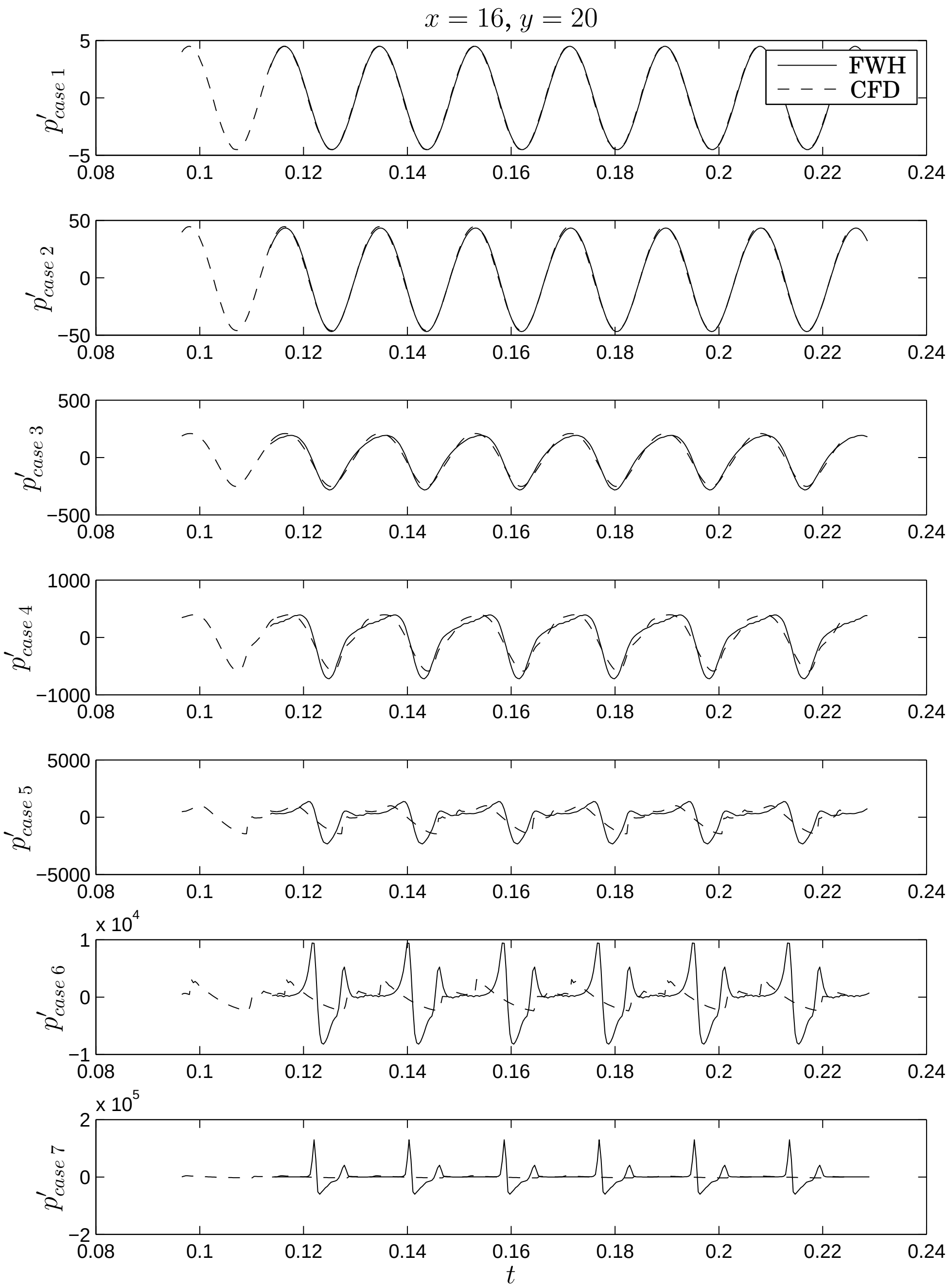

Figure A.6: Pressure fluctuations for cases 1-7 at point "c" in figure A.2 for both the FWH prediction and CFD data

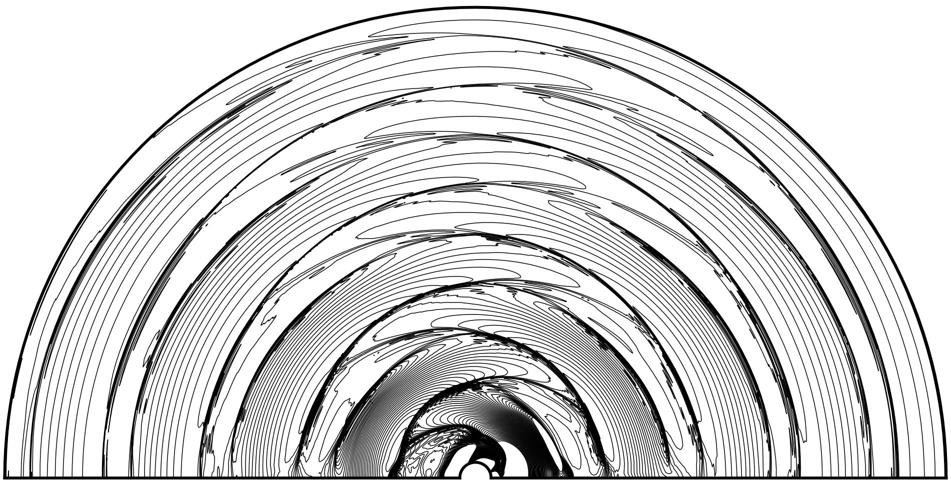

Figure A.7: Instantaneous contours of static pressure for case 6. Shocks are formed around the sphere that propagates in the entire domain.

Paper I

Paper II

Paper III

Paper IV

Paper V

Paper VI